

Wake transition and aerodynamics of a dragonfly-inspired airfoil

Alessandro Chiarini^{1,3}  and Gabriele Nastro² 

¹Complex Fluids and Flows Unit, Okinawa Institute of Science and Technology Graduate University, 1919-1 Tancha, Onna-son, Okinawa 904-0495, Japan

²ISAE SUPAERO, Université de Toulouse, France

³Dipartimento di Scienze e Tecnologie Aerospaziali, Politecnico di Milano, via la Masa 34, Milano 20156, Italy

Corresponding authors: Gabriele Nastro, gabriele.nastro@isae-supero.fr; Alessandro Chiarini, alessandro.chiarini@polimi.it

(Received 7 September 2024; revised 12 January 2025; accepted 10 February 2025)

We investigate the dynamics and the stability of the incompressible flow past a corrugated dragonfly-inspired airfoil in the two-dimensional (2-D) $\alpha-Re$ parameter space, where α is the angle of attack and Re is the Reynolds number. The angle of attack is varied in the range of $-5^\circ \leq \alpha \leq 10^\circ$, and Re (based on the free stream velocity and the airfoil chord) is increased up to $Re = 6000$. The study relies on linear stability analyses and three-dimensional (3-D) nonlinear direct numerical simulations. For all α , the primary instability consists of a Hopf bifurcation towards a periodic regime. The linear stability analysis reveals that two distinct modes drive the flow bifurcation for positive and negative α , being characterised by a different frequency and a distinct triggering mechanism. The critical Re decreases as $|\alpha|$ increases, and scales as a power law for large positive/negative α . At intermediate Re , different limit cycles arise depending on α , each one characterised by a distinctive vortex interaction, leading thus to secondary instabilities of different nature. For intermediate positive/negative α , vortices are shed from both the top/bottom leading- and trailing-edge shear layers, and the two phenomena are frequency locked. By means of Floquet stability analysis, we show that the secondary instability consists of a 2-D subharmonic bifurcation for large negative α , of a 2-D Neimark–Sacker bifurcation for small negative α , of a 3-D pitchfork bifurcation for small positive α and of a 3-D subharmonic bifurcation for large positive α . The aerodynamic performance of the



Downloaded from <https://www.cambridge.org/core>. IP address: 160.79.111.135, on 23 Apr 2025 at 00:32:01, subject to the Cambridge Core terms of use, available at <https://www.cambridge.org/core/terms>. <https://doi.org/10.1017/jfm.2025.205>

dragonfly-inspired airfoil is discussed in relation to the different flow regimes emerging in the $\alpha-Re$ space of parameters.

Key words: wakes

1. Introduction

Over the years, the structure of the wings of animals like insects, birds and bat flies has attracted the attention of many scholars, because of its relevance that goes beyond a fundamental interest to encompass emerging engineering applications such as micro air vehicles (MAVs) and unmanned aerial vehicles (UAVs) (Kang & Shyy 2013; Liu *et al.* 2016). These vehicles typically operate over a wide range of Reynolds numbers (Re), $Re \approx 10^2-10^5$, and face distinctive challenges in generating sufficient aerodynamic forces to sustain flight and perform complex manoeuvres. Many bio-inspired vehicle designs have been proposed, including fixed-, rotary- and flapping-wing configurations (Phan & Park 2019). Mimetics in bio-inspired flight systems can indeed offer new insights and breakthrough technologies in the fields of low-speed aerodynamics and flight control.

1.1. Dragonfly-inspired airfoil

In this context, dragonflies (see [figure 1a](#)) have always drawn a great deal of interest, inspiring many biomimetic flying robots. Dragonfly wings are not smooth or simple cambered surfaces (see for instance the numerical reconstruction of a dragonfly wing in [figure 1d](#) of Bomphrey *et al.* 2016). As illustrated in [figure 1\(b\)](#), the wing cross-section is highly irregular and low-cambered and varies significantly along the spanwise direction (Okamoto, Yasuda & Azuma 1996). Dragonfly wings present high stiffness and strength, and exhibit excellent aerodynamic performance due to their extremely corrugated configuration (Jongerius & Lentink 2010). Moreover, in contrast to other four-winged insects, the fore and hind wings of dragonflies work independently. This double flight-power system allows large dragonflies to perform complex manoeuvres (Rüppell 1989) and gliding flight (Wakeling & Ellington 1997). Thanks to their unique aerodynamic characteristics, dragonfly-inspired wings are widely spread and studied (Newman, Savage & Schouella 1977; Rüppell 1989; Wakeling & Ellington 1997; Kesel 2000; Levy & Seifert 2009; Bomphrey *et al.* 2016; Bauerheim & Chapin 2020), especially in the context of the MAVs/UAVs research area. They indeed represent a relevant configuration of study in the perspective of tandem-wings and flapping flight (see §§ 3 and 4 of Bomphrey *et al.* 2016). However, despite the interest, even the gliding-flight dynamics of an isolated cross-section profile is not entirely clear, and the link between the flow dynamics and the enhanced aerodynamic performance in the complete $\alpha-Re$ parameter space requires further investigation.

Several profile models that replicate the general dragonfly-wing cross-section have been introduced over the years. In this work, we consider the cross-section model introduced by Newman *et al.* (1977) and later used by other authors (see for example Levy & Seifert 2009; Bauerheim & Chapin 2020). As illustrated in [figure 1\(c\)](#), this simplified dragonfly-inspired configuration exhibits two sharp-corner corrugations with a rear arc that combines the mean geometrical characteristics of the profile cross-sections of dragonfly fore and hind wings. The coordinates of some points along the lower surface are presented in [table 1](#) and the thickness t is 0.5 % of the chord c .

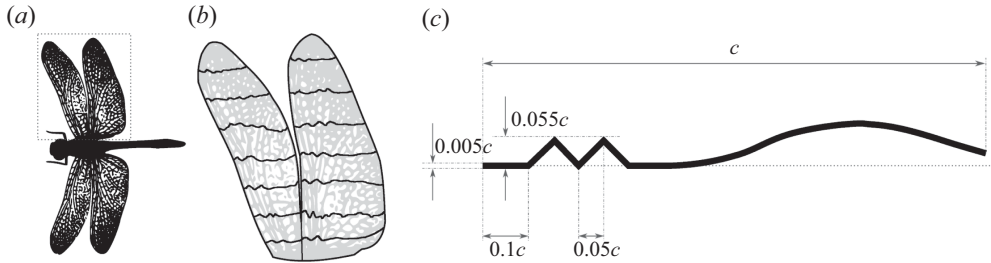


Figure 1. Drawing of (a) a dragonfly and (b) close-up inset of its fore- and hind wings whose profile cross-sections are qualitatively depicted in black (see also Kesel 2000; Bomphrey *et al.* 2016). Geometry of (c) a simplified dragonfly airfoil based on the work of Newman *et al.* (1977) about gliders.

	P_1	P_2	P_3	P_4	P_5	P_6	P_7	P_8	P_9	P_{10}	P_{11}	P_{12}	P_{13}	P_{14}	P_{15}	P_{16}
x_b/c	0	0.09	0.14	0.19	0.24	0.29	0.34	0.5	0.6	0.7	0.75	0.8	0.85	0.9	0.95	1
y_b/c	0	0	0.055	0	0.055	0	0	0.02	0.06	0.08	0.085	0.08	0.07	0.055	0.04	0.025

Table 1. Coordinates (x_b, y_b) of the bottom side of the dragonfly-inspired airfoil, made dimensionless with the chord c . The coordinates of the top side (x_t, y_t) are $(x_t, y_t) = (x_b, y_b + t)$, where $t = 0.005c$ is the body thickness.

Levy & Seifert (2009) showed that for $Re \leq 8000$ and $-2^\circ \leq \alpha \leq 10^\circ$, the aerodynamic performance of this two-dimensional (2-D) dragonfly-inspired airfoil is superior to that of similar, but smooth airfoils (e.g. the traditional low- Re airfoil Eppler-E61). In particular, they found that dragonfly-inspired airfoils exhibit a lower drag and a higher aerodynamic efficiency. Bauerheim & Chapin (2020) investigated the dynamics of the flow past this specific corrugated airfoil at $Re = 6000$, varying the angle of attack (α) in the $6^\circ \leq \alpha \leq 10^\circ$ range. Interestingly, they found that a small variation of α may lead to a sudden change of regime and, therefore, to a large variation of the aerodynamic performance. For $7.7^\circ \leq \alpha \leq 8.5^\circ$, they showed a sudden transition to chaos, which has been explained with the complex interaction between the main unstable shear layer produced at the leading-edge and the reverse flow in the cavity between the second corrugation and the rear arc on the suction side. In contrast, for higher α ($\alpha > 8.5^\circ$), they observed a periodic nonlinear regime. They found that the maximum lift-to-drag ratio is obtained just before the transition to chaos ($\alpha < 7.7^\circ$), whereas the highest lift coefficient is reached in the nonlinear periodic regime ($\alpha > 8.5^\circ$). More recently, Fujita & Iima (2023), considered the corrugated airfoil introduced by Kesel (2000), and investigated by 2-D direct numerical simulations its aerodynamic performance (in an impulsively started configuration) at $Re = 4000$ and $20^\circ \leq \alpha \leq 40^\circ$. They observed that the corrugated geometry enhances the aerodynamic performance when compared with a flat plate, but only for $\alpha > 30^\circ$. They suggest that the mechanisms that are responsible for the lift increase at these large α are (i) the pressure reduction over the top side due to the complex vortex interaction and (ii) the generation of a low-pressure region within the grooves near the leading-edge.

A comprehensive characterisation of the flow around dragonfly-inspired airfoils in a gliding flight configuration in the complete $\alpha-Re$ parameter space is missing, and the understanding of the underlying physics still remains elusive. In this work, we make a step forward in this direction. We use the cross-section geometry introduced by Newman *et al.* (1977) to investigate the sequence of bifurcations the flow undergoes up $Re = 6000$ for

both positive and negative α , and relate the different flow regimes with the (enhanced) aerodynamic performance.

1.2. Two- and three-dimensional wake transition

The flow past smooth airfoils has been largely investigated over the years, with a particular focus on the transition from the steady 2-D wake flow at low Re , to the three-dimensional (3-D) and fully turbulent regime at large Re . The primary instability leads from the low- Re steady state to a periodic vortex street (von Kármán 1954), and consists of a 2-D von Kármán mode that arises from a supercritical Hopf bifurcation (Sreenivasan, Strykowski & Olinger 1987); see He *et al.* (2017), Nastro *et al.* (2023) and Gupta *et al.* (2023) for symmetric and non-symmetric airfoils. Several authors found that the critical Re and α , i.e. the values of Re and α corresponding to the first onset of the primary bifurcation, scale as a power law of α and Re , respectively (Gupta *et al.* 2023; Nastro *et al.* 2023). At larger Re and/or α , the flow past smooth airfoils undergoes a secondary instability and becomes 3-D. Recently, Gupta *et al.* (2023) investigated the three-dimensionalisation of the wake past NACA airfoils at different α . They found that the transition from 2-D to 3-D flow follows a power law $\alpha_{3-D} \sim Re^{-0.5}$, and occurs through a subharmonic (period-doubling) mode, called mode C , having a characteristic spanwise wavelength of $0.1 \lesssim \lambda_z/c \lesssim 0.4$ that increases with α . The same mode has been observed to be responsible of the three-dimensionalisation of the flow past stalled or post-stalled NACA0012 and NACA0015 airfoils (Meneghini *et al.* 2011; Deng, Sun & Shao 2017), and of the flow past inclined flat plates at $20^\circ \leq \alpha \leq 30^\circ$ (Yang *et al.* 2013). Further increasing Re beyond criticality, Deng *et al.* (2017) found via Floquet analysis that further subdominant modes become unstable, i.e. the synchronous mode A , the quasi-periodic mode QP , and the subharmonic modes SL and SS .

The bifurcation scenario valid for smooth NACA airfoils is expected to not hold for non-smooth airfoils. In fact, the shape and the aspect ratio \mathcal{R} (the chord-to-thickness ratio) of the body are known to influence the type and the sequence of bifurcations the flow undergoes. In the simple case of symmetric 2-D bluff bodies in free stream, for example, the nature of the secondary bifurcation changes with the geometry and \mathcal{R} , despite the primary bifurcation consisting of a Hopf bifurcation towards a 2-D and time-periodic state for all cases (Jackson 1987; Chiarini *et al.* 2022b). For the circular (Williamson 1988; Barkley & Henderson 1996) and square (Robichaux, Balachandar & Vanka 1999) cylinders, the flow three-dimensionalisation is driven by the synchronous and long-wavelength mode A , while the synchronous mode B , characterised by a shorter wavelength and a different spatio-temporal symmetry, becomes amplified at larger Re (Barkley, Tuckerman & Golubitsky 2000). Further increasing Re , an additional quasi-periodic QP mode with frequency that is not commensurate with that of the periodic base flow arises (Blackburn & Lopez 2003; Blackburn, Marques & Lopez 2005). Mode A drives the 3-D wake transition also for elliptic cylinders with different \mathcal{R} (Leontini, Lo Jacono & Thompson 2015). For rectangular cylinders with aerodynamic leading edge, instead, mode A is the leading mode for $\mathcal{R} < 7.5$ only (Ryan, Thompson & Hourigan 2005). For larger \mathcal{R} , the flow three-dimensionalisation is instead driven by the so-called mode B' , which possesses the same spatio-temporal symmetries as mode B , but has a much larger wavelength. For rectangular cylinders with sharp corners and $\mathcal{R} \leq 1$, mode A drives the flow three-dimensionalisation for $\mathcal{R} \geq 0.1$ only (Choi & Yang 2014). For smaller \mathcal{R} , the flow three-dimensionalisation is due to the so-called mode $QP2$, which differs from mode QP due to the larger wavelength. For elongated cylinders, i.e. $\mathcal{R} \sim 5$, Chiarini *et al.* (2022a) found that the scenario further complicates, and that the flow

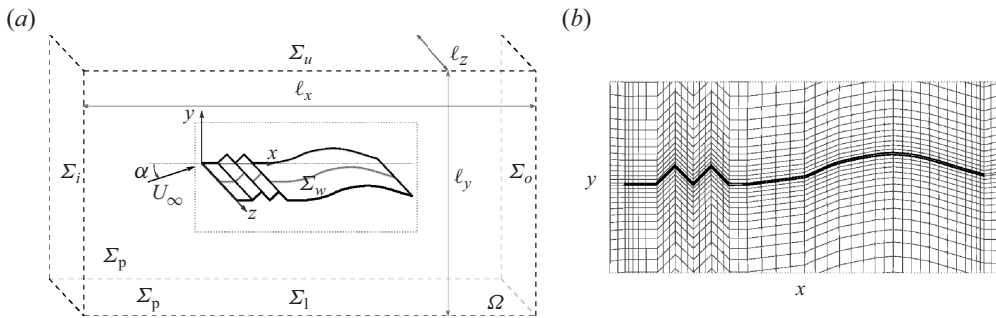


Figure 2. Sketches of (a) the extruded geometry and the flow computational domain for three-dimensional DNS and (b) the grid details in a cross-section (evidenced by the dotted-line rectangle in panel a) around the dragonfly-inspired airfoil.

becomes 3-D due to a quasi-subharmonic mode QS with a characteristic wavelength similar to that of mode A . This bifurcation is triggered by the mutual inviscid interaction between the recirculating regions that coexist over the cylinder side at a given time.

1.3. Focus of the present work

In this work, we consider a dragonfly-inspired airfoil and characterise the sequence of bifurcations the flow undergoes in the 2-D space of parameters of α and Re . The aim of the present study is to extend the work of Bauerheim & Chapin (2020) to a wider range of parameters. In particular, we aim to: (i) characterise the sequence of bifurcations the flow undergoes for different values of α as Re increases; (ii) provide a comprehensive description of the flow regimes in the $\alpha - Re$ parameter space; and (iii) relate them to the enhanced aerodynamic performance of the airfoil, with a look at the MAVs and UAVs research field. The angle of attack is varied in the range of $-5^\circ \leq \alpha \leq 10^\circ$, while Re is increased up to $Re = 6000$. The flow behaviour largely changes with Re and α , ranging from a 2-D and steady flow for small Re and/or $|\alpha|$ to a 3-D and non-periodic state at larger Re and/or $|\alpha|$. Based on 2-D and 3-D high-fidelity direct numerical simulation (DNS) and stability analyses, we provide a complete picture of the dynamics around this geometry in a gliding flight configuration, and clarify the different bifurcations experienced by the flow and how they are related to the distinctive aerodynamic performance of the airfoil.

The remainder of the work is organised as follows. The mathematical framework and the numerical methods are presented in § 2. In § 3, the flow regimes are introduced. The primary bifurcation is then addressed in § 4, while the dynamics of the time-periodic flow at intermediate Re and the secondary flow bifurcations are discussed in §§ 5 and 6, respectively. In § 7, we discuss the aerodynamic performance of the corrugated airfoil in relation to the flow regimes and bifurcations. Eventually, a concluding discussion and perspectives are provided in § 8.

2. Methods

2.1. Flow configuration and governing equations

The incompressible flow over a dragonfly-inspired airfoil (see figure 2) is investigated via nonlinear 2-D and 3-D simulations, and stability analyses. The geometry considered in this work is modelled by extruding the two-dimensional profile introduced by Newman *et al.* (1977), which has been largely used to study the flow past dragonfly-inspired wings in different regimes (Levy & Seifert 2009; Bauerheim & Chapin 2020). The geometry is

discretised after a linear interpolation of the 32 points shown in table 1, 16 for each airfoil side; the geometry has thickness $t = 0.005c$ (c is the chord) and sharp corners. It has been verified that a spline-type interpolation between the 32 points gives the same results in the considered range of α and Re . A Cartesian reference system is placed at the leading edge of the airfoil, with the x -axis being aligned with the airfoil chord and the y - and z -axes denoting the vertical and spanwise directions, respectively.

The Newtonian fluid flow is governed by the incompressible Navier–Stokes (NS) equations for the velocity $\mathbf{u} = (u, v, w)$ and pressure p fields:

$$\frac{\partial \mathbf{u}}{\partial t} + \mathbf{u} \cdot \nabla \mathbf{u} = -\nabla p + \frac{1}{Re} \nabla^2 \mathbf{u}, \quad \nabla \cdot \mathbf{u} = 0. \quad (2.1)$$

The NS equations (2.1) are completed with the following boundary conditions: an undisturbed uniform velocity is assumed at the inlet Σ_i and on the lower and upper boundaries Σ_l and Σ_u , a stress-free boundary condition $p\mathbf{n} - Re^{-1}\nabla \mathbf{u} \cdot \mathbf{n} = 0$ at the outlet Σ_o , periodic conditions on the lateral boundaries Σ_p , and no-slip and no-penetration conditions on the solid walls Σ_w .

The angle of attack α , i.e. the angle between the incoming flow $\mathbf{U}_\infty = (U_\infty \cos(\alpha), U_\infty \sin(\alpha), 0)$ and the x -axis, is varied in the range of $-5^\circ \leq \alpha \leq 10^\circ$. The Reynolds number based on the chord c of the airfoil and the free stream velocity magnitude U_∞ is increased up to $Re = U_\infty c / \nu = 6000$ (ν is the fluid kinematic viscosity). The Strouhal number describing the oscillating flow mechanisms is defined as $St = fc / U_\infty$ with f being the frequency. The drag and lift forces are reported in their non-dimensional form through

$$C_d = \frac{D}{\frac{1}{2}\rho U_\infty^2 c} \quad \text{and} \quad C_\ell = \frac{L}{\frac{1}{2}\rho U_\infty^2 c}, \quad (2.2)$$

where D and L are the aerodynamic forces per unit width in directions parallel and perpendicular to the free stream, respectively, and ρ is the constant fluid density. To describe the aerodynamic performance, it is useful to introduce the aerodynamic efficiency, i.e. the lift-to-drag ratio $E = L/D$.

2.2. Primary instability

The onset of the primary two-dimensional instability is studied using linear theory, which is based on a normal-mode analysis (Theofilis 2003, 2011). The field $\{\mathbf{u}, p\}$ of velocity and pressure is divided into a time-independent base flow $\{\mathbf{U}_1, P_1\}$, and an unsteady contribution $\{\mathbf{u}_1, p_1\}$ with small amplitude ϵ ,

$$\mathbf{u}(\mathbf{x}, t) = \mathbf{U}_1(\mathbf{x}) + \epsilon \mathbf{u}_1(\mathbf{x}, t) \quad \text{and} \quad p(\mathbf{x}, t) = P_1(\mathbf{x}) + \epsilon p_1(\mathbf{x}, t). \quad (2.3)$$

Using this decomposition in the NS equations (2.1), the steady two-dimensional NS equations for $\{\mathbf{U}_1, P_1\}$ are obtained at order ϵ^0 . The governing equations for the small perturbations $\{\mathbf{u}_1, p_1\}$, instead, are obtained at order ϵ^1 , and are the linearised Navier–Stokes (LNS) equations. Using the normal-mode ansatz $\{\mathbf{u}_1, p_1\} = \{\hat{\mathbf{u}}_1, \hat{p}_1\} e^{\gamma t} + c.c.$ ($c.c.$ stands for complex conjugate), the LNS equations yield an eigenvalue problem for the complex eigenvalue $\gamma_1 = \sigma_1 + i\omega_1$ – with σ_1 being the temporal growth rate and ω_1 the angular frequency – and the complex eigenvector $\{\hat{\mathbf{u}}_1, \hat{p}_1\}$,

$$\gamma_1 \hat{\mathbf{u}}_1 + \mathbf{U}_1 \cdot \nabla \hat{\mathbf{u}}_1 + \hat{\mathbf{u}}_1 \cdot \nabla \mathbf{U}_1 = -\nabla \hat{p}_1 + \frac{1}{Re} \nabla^2 \hat{\mathbf{u}}_1, \quad \nabla \cdot \hat{\mathbf{u}}_1 = 0. \quad (2.4)$$

The linear stability of the system is determined by the sign of the real part of γ_1 . If all $\sigma_1 < 0$, the perturbations decay and the flow is linearly stable. If at least one $\sigma_1 > 0$ exists,

the perturbations grow exponentially and the flow is linearly unstable. The imaginary part ω_1 determines whether the time-independent base flow $\{U_1, P_1\}$ experiences a pitchfork or transcritical ($\omega_1 = 0$) or Hopf-type ($\omega_1 \neq 0$) bifurcation. Like for low- Re smooth airfoils (He *et al.* 2017; Nastro *et al.* 2023), for all α considered in this work, the primary instability is due to a 2-D oscillatory mode which arises from a Hopf bifurcation and leads to a time-periodic flow, i.e. a limit cycle solution.

2.3. Secondary instability

When the Reynolds number (or the angle of attack) is above the critical value Re_{c1} (or α_{c1} , respectively), the flow approaches a 2-D periodic limit cycle. The Floquet theory is then used to study the linear stability of the 2-D and time-periodic base flows with respect to 2-D and 3-D perturbations. The flow is written as the sum of a 2-D base flow $\{U_2, P_2\}$, which is periodic with period T , and an unsteady 3-D perturbation with small amplitude ϵ , i.e.

$$\{\mathbf{u}, p\}(x, y, z, t) = \{U_2, P_2\}(x, y, t) + \frac{\epsilon}{\sqrt{2\pi}} \int_{-\infty}^{\infty} \{\mathbf{u}_2, p_2\}(x, y, \beta, t) e^{i\beta z} d\beta, \quad (2.5)$$

where i is the imaginary unit, \mathbf{u}_2 and p_2 indicate the Fourier transform of the velocity and pressure disturbances in the homogeneous spanwise direction z , and $\beta = 2\pi/\lambda_z$ is the corresponding wavenumber, with λ_z being the wavelength.

Introducing the decomposition (2.5) into the NS equations (2.1), the 2-D periodic base flow is obtained at order ϵ^0 , while the eigenproblem describing the linear evolution of the perturbations is obtained at order ϵ^1 . By applying the Fourier transform in the z direction, the unsteady linearised Navier–Stokes equations for each β read

$$\frac{\partial \mathbf{u}_2}{\partial t} + U_2 \cdot \nabla_{\beta} \mathbf{u}_2 + \mathbf{u}_2 \cdot \nabla_{\beta} U_2 - \frac{1}{Re} \nabla_{\beta}^2 \mathbf{u}_2 + \nabla_{\beta} p_2 = 0, \quad \nabla_{\beta} \cdot \mathbf{u}_2 = 0. \quad (2.6)$$

Here, $\nabla_{\beta} \equiv (\partial/\partial x, \partial/\partial y, i\beta)$ is the Fourier-transformed gradient operator. Following the Floquet theory, we assume the functional form for the perturbation field $\{\mathbf{u}_2, p_2\}$ given by

$$\{\mathbf{u}_2, p_2\}(x, y, \beta, t) = \{\hat{\mathbf{u}}_2, \hat{p}_2\}(x, y, \beta, t) e^{\gamma t}, \quad (2.7)$$

where $\gamma = \sigma_2 + i\omega_2$ is the Floquet exponent and $\{\hat{\mathbf{u}}_2, \hat{p}_2\}$ is the Floquet mode associated with γ_2 and β , and possesses the same periodicity of the base flow

$$\{\hat{\mathbf{u}}_2, \hat{p}_2\}(x, y, \beta, t + T) = \{\hat{\mathbf{u}}_2, \hat{p}_2\}(x, y, \beta, t). \quad (2.8)$$

The stability of the system is determined by the sign of σ_2 or, equivalently, by the modulus of the Floquet multiplier $\mu = e^{\gamma_2 T}$. If all $\sigma_2 < 0$ or $|\mu| < 1$, the perturbations decay and the flow remains two-dimensional and periodic. Otherwise, if at least one exponent exists with $\sigma_2 > 0$ or $|\mu| > 1$, the perturbations grow exponentially and the flow bifurcates becoming 3-D if $\beta \neq 0$ or remaining 2-D if $\beta = 0$. Bifurcations of the limit cycle solution depend on how the corresponding Floquet multiplier crosses the unit circle in the complex plane. If $\mu = +1$, the periodic orbit presents a (secondary) pitchfork or saddle-node bifurcation yielding a new stable limit cycle with the same period as the starting one. If $\mu \neq +1$, i.e. $\omega_2 \neq 0$, a new frequency emerges and the resulting flow attractor draws a torus in the phase space. This bifurcation is called secondary Hopf or Neimark–Sacker bifurcation. As Neimark–Sacker bifurcations introduce a new temporal frequency, in general incommensurate with that of the original orbit, the resulting solutions are referred to as temporally quasi-periodic. Within this case (i.e. $\omega_2 \neq 0$), the particular condition $\mu = -1$, i.e. $\omega_2 = \omega_1/2$ with ω_1 the base flow angular frequency, is called

period-doubling, flip or subharmonic bifurcation. In this case, the bifurcation leads to a new limit cycle that presents twice the periodicity of the starting one.

2.4. Numerical methods

Two different numerical methods are used. The 3-D DNS and the primary instability analysis are carried out using the open source high-performance solver Nek5000 (Fischer, Lottes & Kerkemeier 2008), which is based on spectral elements. The secondary stability analysis is instead based on finite elements and the simulations have been implemented in the non-commercial software FreeFem++ (Hecht 2012).

The spatial discretisation for the nonlinear 3-D simulations relies on a square-grid mesh (see figure 2). The streamwise, cross-stream and spanwise extents are set to $\ell_x = 20c$, $\ell_y = 20c$ and $\ell_z = c$, respectively. The choice of $\ell_z = c$ is justified by the fact that the 3-D modes that emerge and drive the dynamics in the considered range of Re are characterised by $\beta \geq 2\pi/c$ (see § 6). The grid consists of approximately 1.2×10^6 spectral elements with polynomial order $P = 6$. The total number of degrees of freedom N_{dof} is thus approximately 2.6×10^8 . A semi-implicit third-order accurate temporal scheme is used to integrate forward in time the NS equations with a target CFL of 0.5 (see Fischer *et al.* 2008, for more detail). Numerical simulations were performed for a final time greater than or equal to 200 convective time scales to ensure the complete settlement of the flow regime.

Primary instability results are also obtained with Nek5000. The low- Re steady two-dimensional base flow \mathbf{U}_1 is obtained using the selective frequency damping (SFD) method proposed by Åkervik *et al.* (2006), wherein the NS steady solution is obtained by damping the unstable frequency via the addition of a dissipative relaxation term proportional to the frequency content of the velocity oscillations. The generalised eigenvalue problem (2.4) for the onset of the primary instability is solved via Krylov techniques described extensively in § 3 of Frantz, Loiseau & Robinet (2023). Consistently with the 3-D DNS, the computational domain extends for $(\ell_x, \ell_y) = (20c, 20c)$. The grid consists of 2.24×10^5 spectral elements with polynomial order $P = 6$, yielding a total number of degrees of freedom of $N_{dof} \approx 8.06 \times 10^6$. The convergence of the results is discussed in Appendix B, § B.1.

The results of the secondary stability analysis are obtained with the numerical code used and validated by Chiarini *et al.* (2022a), which is based on finite elements. The finite-element formulation employs quadratic elements (P2) for the velocity and linear elements (P1) for the pressure. The 2-D periodic base flow \mathbf{U}_2 is computed integrating in time the 2-D version of the unsteady NS equations. The time integration employs an explicit third-order low-storage Runge–Kutta method for the nonlinear term, combined with an implicit second-order Crank–Nicolson scheme for the linear terms (Rai & Moin 1991). The BoostConv algorithm is used to accelerate the convergence of the nonlinear simulations to the periodic limit cycle. It is an iterative algorithm inspired by the Krylov subspace methods introduced by Citro *et al.* (2017). Convergence is reached when the absolute value of the largest difference over the computational domain between variables at t and $t + T$ is below 10^{-10} . The numerical method used for the Floquet analysis is similar to that used in the works by Barkley & Henderson (1996) and Jallas, Marquet & Fabre (2017). The evolution of the velocity perturbation with wavenumber β , i.e. \mathbf{u}_β , from time t_0 to time $t_0 + T$ can be written using the linearised Poincaré map \mathcal{P}_β as

$$\mathbf{u}_\beta(t_0 + T) = \mathcal{P}_\beta \mathbf{u}_\beta(t_0). \quad (2.9)$$

The Floquet multipliers μ_β and the Floquet modes $\hat{\mathbf{u}}_{2,\beta}$ at the time t_0 correspond to the eigenvalues and eigenvector of \mathcal{P}_β . The eigenvalues of \mathcal{P}_β with largest modulus and the

corresponding eigenvectors are computed using the Arnoldi method (Saad 2011), which implies the iterative action of the \mathcal{P}_β operator. The modified Gram–Schmidt algorithm is used for the orthogonalisation of the eigenvectors. All the computed Floquet modes are normalised using their kinetic energy. After solving the eigenvalue problem, we evaluate the evolution of the Floquet mode over the period T by integrating (2.6) using the computed $\{\hat{\mathbf{u}}_{2,\beta}, p_{2,\beta}\}(t_0)$ as initial condition. To account for the time decay/growth (see (2.7)) the result of the integration is corrected by $e^{\lambda_1 t}$. For consistency, the time integration of the linearised Navier–Stokes equations is carried out with the same numerical scheme used for the computation of $\{\mathbf{U}_2, P_2\}$. When integrating the linearised Navier–Stokes equations, we evaluate the base flow at each time step by Fourier interpolation of 100 instantaneous $\{\mathbf{U}_2, P_2\}$ fields stored uniformly along the period T . The adjoint modes needed to compute the structural sensitivities are obtained in a similar way (see Chiarini *et al.* 2022a for additional details). For the secondary stability analysis, two different computational domains have been used, after a preliminary convergence study (see Appendix B, § B.2). For $8^\circ \leq \alpha \leq 10^\circ$, the computational domain extends for $(\ell_x, \ell_y) = (20c, 30c)$ with a number of triangles of $N_{el} \approx 15.4 \times 10^4$. For $-5^\circ \leq \alpha \leq 7^\circ$, instead, the computational domain extends for $(\ell_x, \ell_y) = (17.5c, 14c)$ with $N_{el} \approx 13.8 \times 10^4$. The larger ℓ_y used for the larger α is needed to properly capture the growth rate of the ensuing leading mode (see Appendix B, § B.2). For all cases, the distribution and size of the triangles have been chosen to properly refine the region close to the body, paying particular attention to the near-corner regions and to the wake.

Hereinafter, unless otherwise indicated, all quantities are made dimensionless with U_∞ and c .

3. Flow regimes

A variation of α modifies the low- Re 2-D flow and, therefore, changes the sequence of bifurcations the flow undergoes at larger Re . In this section, we start by using the 3-D nonlinear simulations to identify the different flow regimes in the considered portion of the $\alpha-Re$ space of parameters. The different flow bifurcations and regimes are then characterised in detail in § 4.2 and § 6, by means of stability analyses. In the following, we distinguish between steady, periodic and non-periodic flow regimes. A regime is said to be non-periodic when it is characterised by multiple, distinct, non-commensurate frequencies.

Figure 3 shows the dominant Strouhal number, measured via inspection of the frequency spectrum of the longitudinal velocity probed at $(x, y, z) = (1.3, 0.17, 0.5)$, in the $\alpha-Re$ parameter space. From a qualitative viewpoint, the results are independent of the choice of the probe location. Numerical simulations were run long enough to ensure that the transient was exceeded and that the flow regime was completely settled; considering that the simulations are advanced for at least $200c/U_\infty$ after the initial transient, the frequency resolution is lower than or equal to $\Delta f \sim 6 \times 10^{-3}$, which has been verified to ensure the appropriate depiction of the complete spectrum for each flow regime. The flow regimes are indicated by different symbols in the $\alpha-Re$ map, and are illustrated with representative snapshots in panels (a)–(i).

The lowest contour level in figure 3(a) delimits the threshold for unsteadiness. Below this threshold (i.e. in the white area of the map), the flow is steady and 2-D. Here, the Reynolds number is indeed lower than the critical Reynolds number $Re_{c1}(\alpha)$ which denotes Re corresponding to the first onset of the primary bifurcation at a given α . Here, Re_{c1} decreases as $|\alpha|$ increases, with the maximum value $Re_{c1} \approx 3400$ found for $\alpha = -1^\circ$. Nevertheless, for all α , the primary bifurcation consists of a Hopf bifurcation towards a 2-D periodic limit cycle, characterised by an alternating vortex shedding in the wake.

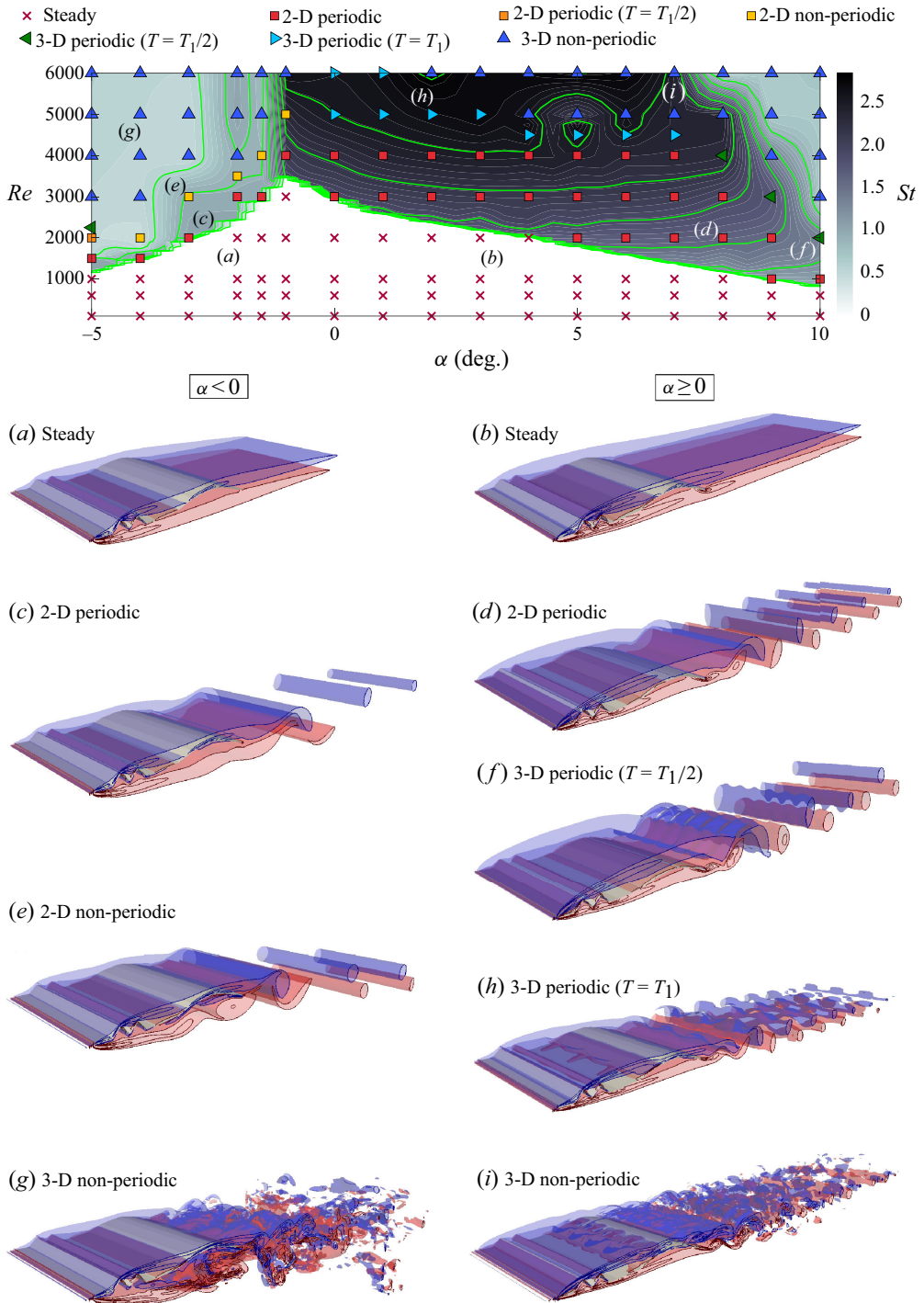


Figure 3. Dominant Strouhal number (measured from the frequency spectrum of the longitudinal velocity probed at $(x, y, z) = (1.3, 0.17, 0.5)$) map from DNS in the $\alpha - Re$ parameter space. Ten equally spaced green-coloured contour levels are used. Symbols indicate the wake regime observed from the results of numerical simulations whose spanwise vorticity is depicted at the bottom. The green left-oriented (blue right-oriented) triangle refers to a periodic 3-D state that arises after a subharmonic (pitchfork) bifurcation of the 2-D periodic regime at lower Re ; see § 6.

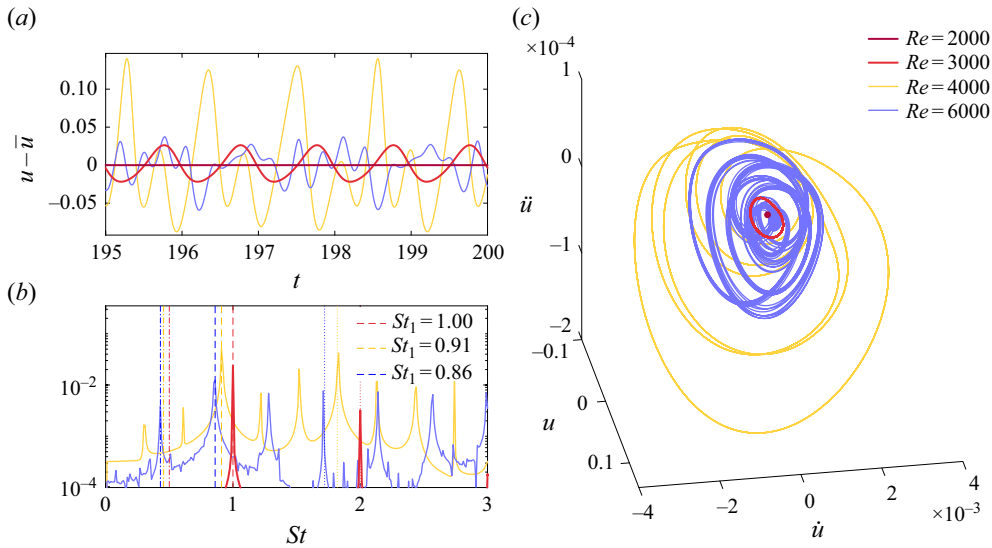


Figure 4. Longitudinal velocity signal at $\alpha = -1.5^\circ$ for different Re : (a) temporal fluctuations of the longitudinal velocity u at $(x, y, z) = (1.3, 0.17, 0.5)$; (b) corresponding spectrum; (c) flow attractor. The $\bar{\cdot}$ operator indicates time average.

As detailed in § 5, different limit cycles arise depending on α , each one characterised by different vortex interactions. This is visualised in figure 3 by the large dependence of the dominant flow frequency on α at intermediate Re ; for $\alpha \lesssim -1.25^\circ$, St is smaller compared with the $\alpha > -1.25^\circ$ cases.

The nature of the secondary bifurcation changes with α . For small negative α ($-5^\circ < \alpha < -1.25^\circ$), the limit cycle becomes unstable via a 2-D Neimark–Sacker bifurcation. At $Re = Re_{c2}$, the wake loses the temporal symmetry due to the emergence of an incommensurate frequency, but retains its 2-D character; see the light orange squares in the α – Re map, and the 2-D non-periodic state depicted in figure 3(e). When increasing Re , the wake becomes first 3-D and then approaches a more chaotic regime. As an example, figure 4 considers $\alpha = -1.5^\circ$, and shows the dependence of the frequency spectrum and of the flow attractor on Re . At $Re = 2000$, the wake is steady, corresponding to a fixed point in the phase space. At $Re = 3000$, instead, the flow is periodic with a vortex-shedding frequency of $St \approx 1$ and a limit cycle arises in the phase space. At $Re = 4000$, several peaks emerge in the frequency spectra and the wake loses its periodic behaviour. A further increase in Re ($Re = 6000$) leads to the flow three-dimensionalisation; see the blue triangles. The redistribution of energy as a result of the three-dimensionalisation promotes a reduction in the amplitude of the longitudinal velocity oscillations in favour of the spanwise velocity oscillations (not shown).

For large negative α ($\alpha \leq -5^\circ$), instead, the secondary bifurcation is 2-D and of subharmonic nature. In this case, a new limit cycle arises for $Re > Re_{c2}$, with twice the periodicity of the original one; see the dark orange square. Before the flow becomes non-periodic for $Re \geq 3000$, this second 2-D limit cycle becomes unstable for $Re > Re_{c3}$ (with $Re_{c3} \approx 2125$ at $\alpha = -5^\circ$) and three-dimensionalises through a 3-D subharmonic bifurcation; see the green left-oriented triangle.

For $0^\circ \leq \alpha \leq 7^\circ$, the secondary instability consists of a 3-D pitchfork bifurcation of the 2-D periodic limit cycle; see the light blue right-oriented triangles. At $Re = Re_{c2}$, the wake becomes 3-D, but retains the same temporal periodicity as at smaller Re .

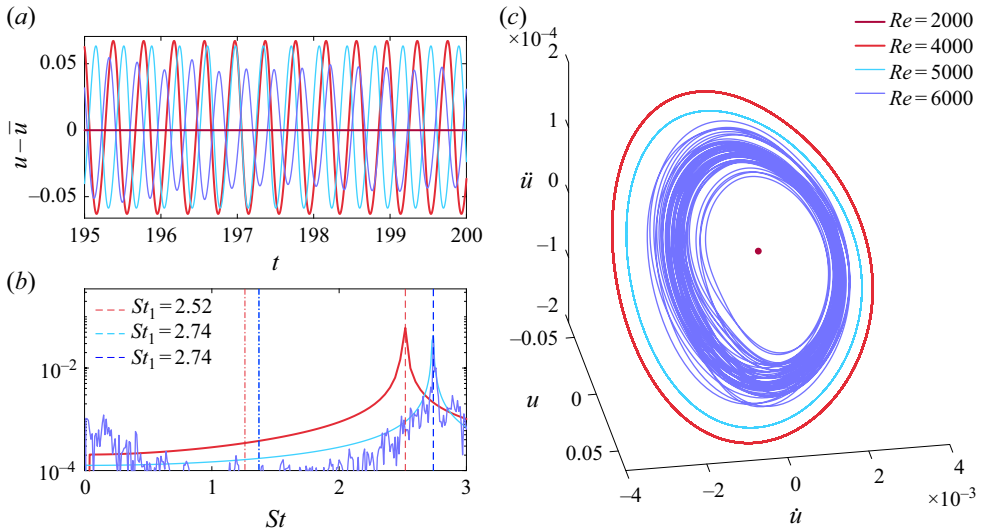


Figure 5. As in figure 4 for $\alpha = 3^\circ$.

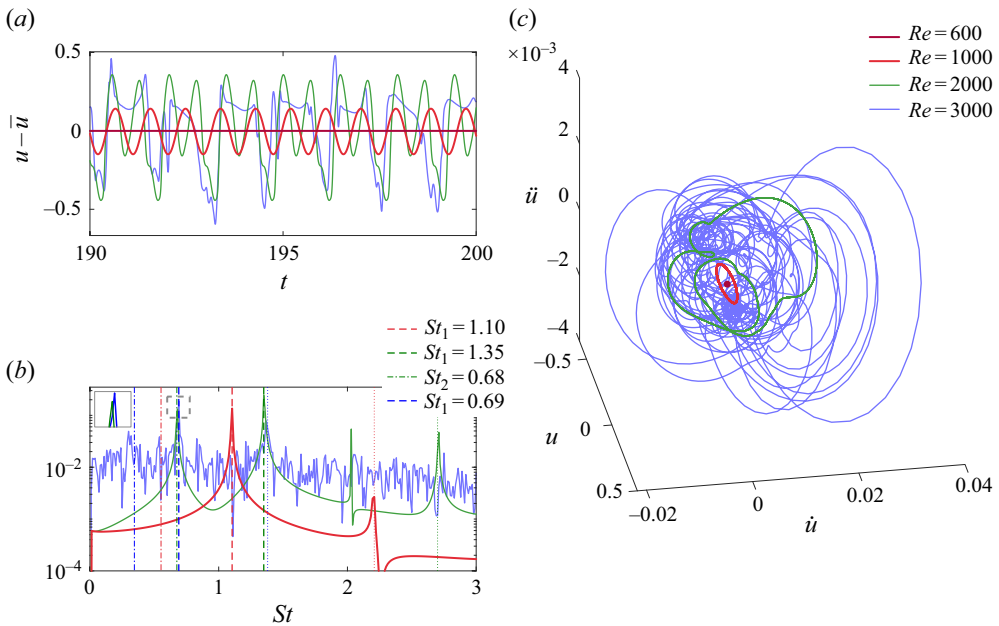


Figure 6. As in figure 4 for $\alpha = 10^\circ$.

Figure 5 considers $\alpha = 3^\circ$ and illustrates the velocity signal for different Re . At $Re = 4000$, the 2-D periodic limit cycle is characterised by a Strouhal number of $St \approx 2.52$. At $Re = 5000$, the spectrum still presents a single peak at $St \approx 2.74$ and the wake becomes 3-D. While retaining the same (slightly larger) dominant frequency $St \approx 2.74$, an increase of Re to $Re = 6000$ yields the emergence of low-frequency beating and the loss of the temporal periodicity of the 3-D wake.

For large positive α (i.e. $\alpha \geq 8^\circ$), the scenario is different; see figure 6 that illustrates the velocity signal at $\alpha = 10^\circ$ at different Re . In this case, the flow remains 2-D and periodic for $Re \lesssim 2000$ with a frequency of $St \approx 1$. At $Re = 2000$, the flow becomes 3-D and a

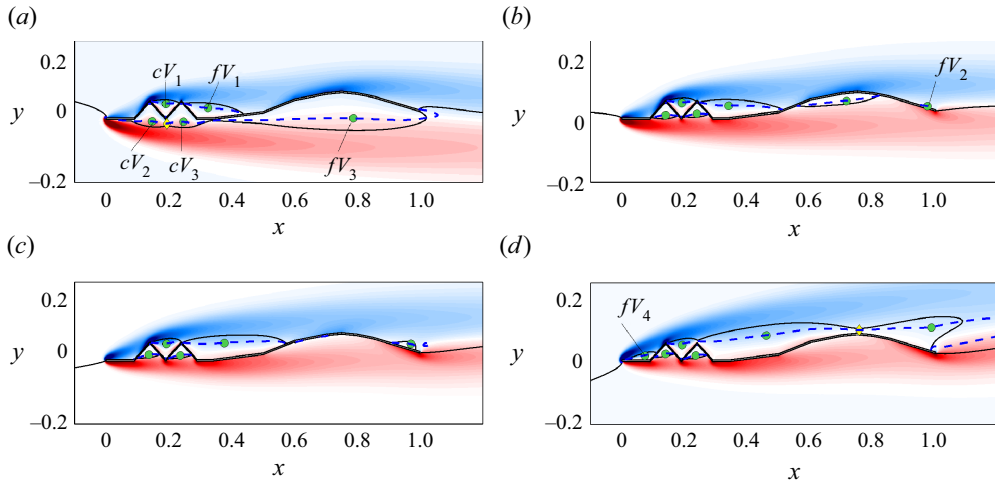


Figure 7. Base flow near the first bifurcation at $Re = 800$. Streamlines are superimposed on the map of the spanwise vorticity $\Omega_{z,1} = \partial V_1/\partial x - \partial U_1/\partial y$, with the blue-to-red colour map in the $-50 \leq \Omega_{z,1} \leq 50$ range: (a) $\alpha = -5^\circ$; (b) $\alpha = 0^\circ$; (c) $\alpha = 5^\circ$; (d) $\alpha = 10^\circ$. Green circles are for the elliptic stagnation points. Yellow diamonds are for the hyperbolic stagnation points. The blue dashed line is for $U_1 = 0$. The tags of the recirculating regions (see text) are introduced only once, in the first panel, the recirculating regions appear.

new peak emerges in the spectrum at half of the vortex-shedding frequency, i.e. $St_2 = St_1/2 = 0.68$. For $\alpha \geq 8^\circ$, indeed, the secondary instability consists of subharmonic 3-D bifurcation of the 2-D periodic limit cycle; see the green left-oriented triangles. Then, when Re is increased up to $Re = 3000$, the flow loses the periodicity and the dominant frequency becomes the subharmonic one, i.e. $St \approx 0.69$ (as evidenced by the close-up view in figure 6b).

4. Low Re : primary bifurcation

In this section, we detail the primary bifurcation of the low- Re steady flow that leads to the 2-D and periodic regime. Both negative and positive α are considered, i.e. $-5^\circ \leq \alpha \leq 10^\circ$.

4.1. Steady base flow

Figure 7 shows the streamlines and vorticity $\Omega_{z,1} = \partial V_1/\partial x - \partial U_1/\partial y$ colour maps of the low- Re steady base flow at $Re = 800$ for $\alpha = -5^\circ, 0^\circ, 5^\circ, 10^\circ$. The stagnation points are marked with symbols. Green circles are used for the elliptical stagnation points corresponding to a local maximum or minimum of the stream function Ψ_1 , defined as $\nabla^2 \Psi_1 = -\Omega_{z,1}$, and are used to detect the centre of rotation of the recirculating regions. Yellow diamonds, instead, refer to hyperbolic stagnation points corresponding to saddle points of Ψ_1 . Quantitative information is provided in figure 8.

Due to the complex geometry, the flow separates in several points, giving origin to many recirculating regions. Some recirculating regions are present at all α and their size only slightly changes with Re . Others, instead, originate only for some values of α and Re , as they are related to pressure gradients that may be stronger/milder and adverse/favourable depending on the flow configuration. We refer to the recirculating regions with size that depends only on the geometry as constrained recirculating regions (cV). The recirculating regions whose size and occurrence depend on α and Re , instead, are referred to as free recirculating regions (fV).

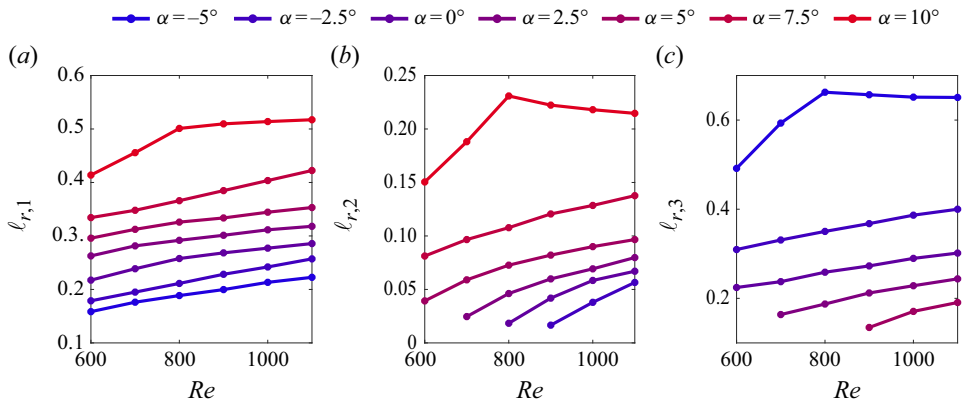


Figure 8. Dependence of the length of the main base flow recirculating regions on Re . See text for the definition of $\ell_{r,1}$, $\ell_{r,2}$ and $\ell_{r,3}$. The size of the recirculating regions are measured using the delimiting $\Psi = 0$ line; when the $\Psi = 0$ line delimits two recirculating regions (see for example figure 7d), the position of the ensuing hyperbolic stagnation point is used as the delimiting point.

Along the top side of the body, a constrained recirculating region (cV_1) is detected close to the leading edge (LE), within the cavity delimited by the two corrugations. Moving downstream, the flow separates from the corner of the downstream groove and reattaches along the body: a large free recirculating region fV_1 arises, with size $\ell_{r,1}$ that monotonically increases with Re and α (see figure 8). Further moving downstream, the flow faces an adverse pressure gradient and, for some values of α and Re , it separates and gives rise to a second free recirculating region fV_2 close to the trailing edge (TE). The separating point of fV_2 moves downstream as α and/or Re increase, and its size $\ell_{r,2}$ monotonically increases with α and Re (see figure 8). Moving to the bottom side, two constrained recirculating regions (cV_2 and cV_3) arise close to the LE within the two grooves. Moving downstream, a further large recirculating region (fV_3) arises depending on Re and α . Its size $\ell_{r,3}$ increases with Re , but decreases with α (see figure 8): for large positive α and small enough Reynolds numbers, it is not detected. Note that over the top side of the body, a further free recirculating (fV_4) region arises for large α and Re , in the area upstream the first corrugation.

When fixing α , the increase of the size of the free recirculating regions with Re is consistent with what is observed for 2-D and 3-D bluff bodies (see for example Giannetti & Luchini 2007; Marquet & Larsson 2015).

4.2. Critical Reynolds number and global modes

We now move to the results of the linear stability analysis. For each α , we consider the steady base flow and look for the growing eigenmodes as Re increases. Figure 9 summarises the effect of α on the first bifurcation; figure 9(a) shows the neutral curves, while figure 9(b) depicts the dependence of the critical frequency of the unstable modes on α . As mentioned in § 3, for all α , the first instability consists of a Hopf bifurcation towards a 2-D and oscillatory state, characterised by an alternating vortex-shedding in the wake. Three unstable modes are detected, i.e. modes pA , pB and pC , with pA and pC being the leading modes for $\alpha \leq -1.25^\circ$ and $\alpha > -1.25^\circ$, respectively. The spatial structure of the modes is shown in figure 10(a, c, e).

For $\alpha \leq -1.25^\circ$, two bifurcations of the steady base flow are found to occur in short sequence. They correspond to the oscillatory modes pA and pB , which are characterised by a different frequency, i.e. $f_{c1_{pA}} \approx 1$ and $f_{c1_{pB}} \approx 0.07$. For all negative α , mode pA

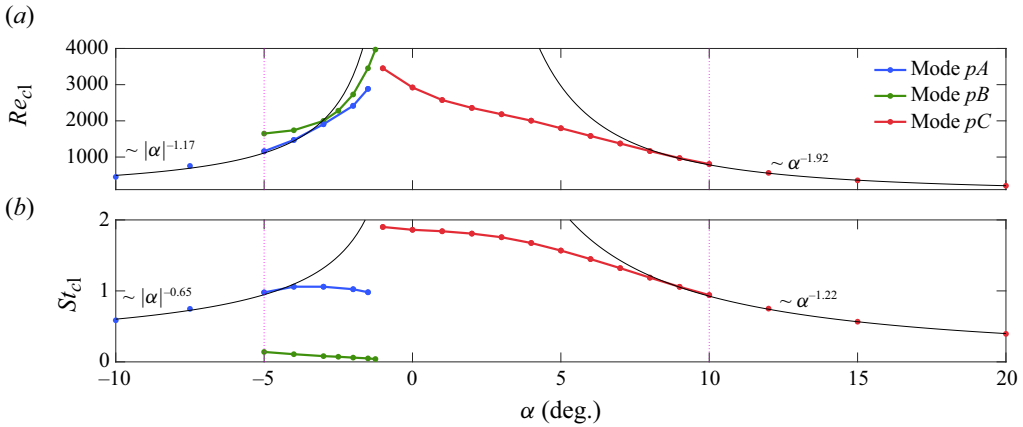


Figure 9. (a) Critical Reynolds number for $-10^\circ \leq \alpha \leq 20^\circ$. (b) Critical frequency of the primary bifurcations.

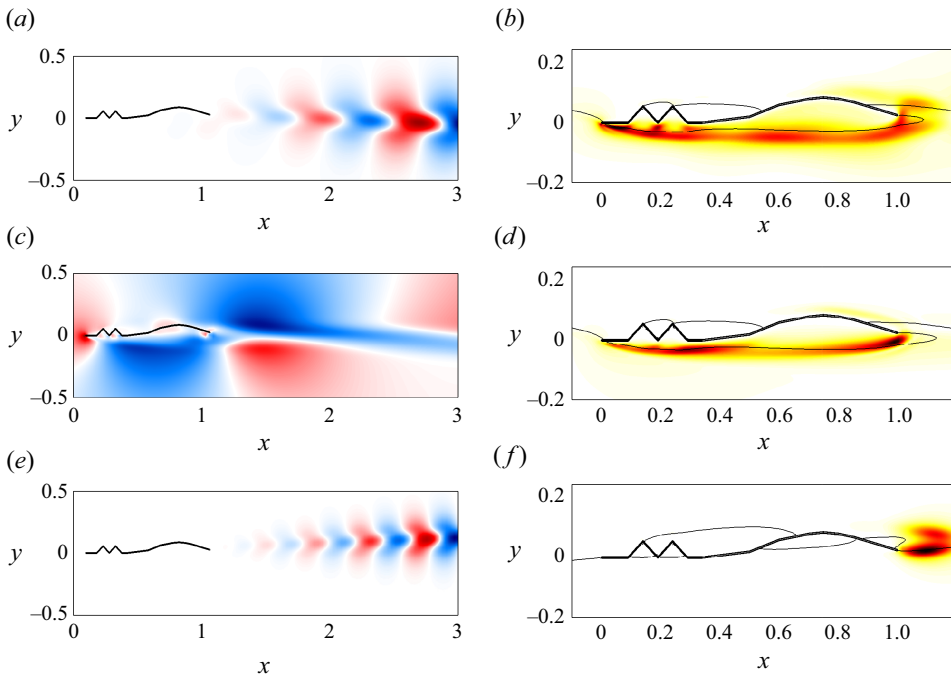


Figure 10. Spatial structure of the leading eigenmodes of the low- Re steady base flow at $Re = Re_{cl}$: (a, c, e) \hat{v}_1 ; (b, d, f) structural sensitivity; (a, b) mode pA for $\alpha = -3^\circ$; (c, d) mode pB for $\alpha = -3^\circ$; (e, f) mode pC for $\alpha = 3^\circ$. The spatial structure of the pA and pB modes (pC mode) does not change qualitatively with α for $-5^\circ \leq \alpha \leq -1.25^\circ$ ($-1.25 < \alpha \leq 10^\circ$).

exhibits a positive growth rate σ_1 for smaller Reynolds numbers with respect to mode pB , i.e. it emerges first as primary instability. For more negative α , the critical Reynolds number of both modes pA and pB decreases and the flow becomes less stable. This is consistent with the increase of the size of the fV_3 recirculating region (where the mechanism triggering the instability is placed; see the following discussion) and with the stronger reverse flow that arises in it. In fact, the size of the recirculating region dictates the spatial extent of the absolute instability pocket (Chomaz 2005) and the intensity of

the reverse flow within it impacts the local amplification of the growing wave packets (Hammond & Redekopp 1997). The spatial structure of the mode pB is largely different from that of the Kármán-like mode pA (see figure 10). Unlike modes pA and what is observed for the flow past other 2-D bluff bodies (Giannetti & Luchini 2007; Chiarini, Quadrio & Auteri 2021), the magnitude of mode pB is large also close to the body sides, particularly within the fV_3 recirculating region. We anticipate that, although pB is an amplified mode of the low- Re steady flow and becomes amplified for $Re > Re_{c1}$ only, it actually emerges in the nonlinear unsteady simulations at Reynolds numbers close to those predicted by the linear stability analysis (see figure 3 and § 6).

For $\alpha > -1.25^\circ$, the scenario changes and the leading mode is mode pC . This agrees with a substantial change of the base flow (see figure 8). Like mode pA for negative α , mode pC is also oscillatory and leads to a vortex shedding in the wake. In this case, the frequency is larger and at criticality, i.e. for $Re = Re_{c1}(\alpha)$, decreases with α , being $f_{c1,pC} \approx 2$ for small α and $f_{c1,pC} \approx 1$ for $\alpha \approx 10^\circ$. The critical Reynolds number decreases when increasing α , in agreement with the enlargement of the fV_2 recirculating region. In the wake, the spatial structure of the mode resembles that of mode pA , but the streamwise wavelength of the wake is smaller in agreement with the larger shedding frequency (see figure 10).

For large positive and negative α , the critical Reynolds number Re_{c1} for modes pA and pC scales as a power law of α , similarly to what was found by other authors for smooth NACA airfoils (Gupta *et al.* 2023; Nastro *et al.* 2023). For mode pA , we find $Re_{c1} \sim |\alpha|^{-1.17}$, while for mode pC , $Re_{c1} \sim \alpha^{-1.92}$. A power law has been observed also for the associated frequencies at criticality, being $f_{c1} \sim |\alpha|^{-0.65}$ for mode pA and $f_{c1} \sim \alpha^{-1.22}$ for mode pC .

In passing, note that the stabilisation of the flow for small values of $|\alpha|$ is consistent with previous results in the literature, which report a monotonic increase of the critical Reynolds number with the streamwise extent of the bodies; see for example Chiarini *et al.* (2022b) and Jackson (1987) for 2-D symmetric bodies, and Zampogna & Boujo (2023) and Chiarini & Boujo (2024) for 3-D rectangular prisms. In fact, for small $|\alpha|$, the characteristic size of the body, once projected in the streamwise direction, increases.

We now look at the structural sensitivity of the modes pA , pB and pC . Figure 10(b, d, f) shows the map of

$$S(\mathbf{x}) = \frac{\|\hat{\mathbf{u}}_1(\mathbf{x})\| \|\hat{\mathbf{u}}_1^\dagger(\mathbf{x})\|}{\int_{\Omega} (\hat{\mathbf{u}}_1^{\dagger*} \cdot \hat{\mathbf{u}}_1) d\Omega}, \quad (4.1)$$

where $\hat{\mathbf{u}}_1^\dagger$ is the adjoint mode and the \cdot^* superscript indicates the complex conjugate. The structural sensitivity was introduced by Giannetti & Luchini (2007) as an upper bound for the eigenvalue variation $|\delta\gamma_1|$ induced by a specific perturbation of the LNS operator. It is a ‘force-velocity coupling’ representing a feedback from a localised velocity sensor to a localised force actuator at the same location. The structural sensitivity is thus an indicator of the eigenvalue’s sensitivity and identifies the wavemaker (Monkewitz, Huerre & Chomaz 1993). The most sensitive regions, where the direct and adjoint modes overlap, are found close to the body for all three modes, which is typical of 2-D and 3-D bluff body wakes; see Giannetti & Luchini (2007), Zampogna & Boujo (2023) and Chiarini & Boujo (2024).

Modes pA and pB are most sensitive along the streamline that separates from the bottom LE corner. In both cases, the structural sensitivity does not show a localised peak, but it is large along a relatively wide region suggesting the existence of a non-local feedback in the ensuing triggering mechanism. For mode pA , the structural sensitivity peaks close to the LE, while for mode pB , the maximum value is found close to the TE.

Also, downstream of the TE, the structural sensitivity of mode pA resembles what was found for the flow past 2-D bluff bodies (Giannetti & Luchini 2007), with the classical structure with two symmetric lobes placed in correspondence of the $\Psi_1 = 0$ line. Mode pC , instead, is most sensitive in the region just downstream of the TE, with the classical double-lobed conformation. For this mode, the intensity of the structural sensitivity is not symmetric being larger within the bottom lobe. This is typical for non-symmetric configurations (see also Chiarini & Auteri 2023; Nastro *et al.* 2023) and indicates that the instability is mainly triggered by the bottom shear layer where the flow faces a larger acceleration. For mode pC , the structural sensitivity is negligible over the lateral sides of the body, indicating that the fV_1 and fV_3 recirculating regions do not play a significant role in the triggering mechanism, and that it is a leading mode of the wake.

The different structural sensitivities found for modes pA and pC indicate that the physical mechanism that drives these two instabilities is not the same: it appears that for mode pA , the mechanism is not confined in the near wake, but involves also the shear layer that separates from the bottom LE corner. For negative α , indeed, the flow separates at the LE and reattaches at the TE, resulting in a ‘long-type’ bubble that encompasses the entire bottom side of the airfoil. However, for mode pC , the absolute instability pocket is embedded in the fV_2 recirculating region in the near wake; for $\alpha \geq -1.25$, the flow does not separate at the bottom LE corner. Accordingly, the characteristic temporal frequencies of the two modes are distinct and exhibit a different dependence on α . The frequency of mode pA is lower ($f \approx 1$) and only marginally varies with α ; for $\alpha < 0$, the extent of the ‘long-type’ bubble does not depend on α . The frequency of mode pC , instead, is larger ($1 \lesssim f \lesssim 2$) and decreases for larger α ; the fV_2 recirculating region enlarges as α increases (see figure 8).

Figure 11 shows the neutral curves of modes pA , pB and pC using alternative definitions of the Reynolds and Strouhal numbers that, in analogy to what is often done in the context of low- Re flows over smooth airfoils and flat plates (see for example Fage & Johansen 1927), are based on a measure of the frontal dimension of the body. Here, we use $d = c \sin(\alpha)$ and h , i.e. the cross-stream projection of the chord and of the airfoil height (Levy & Seifert 2009) (see figure 11a) and introduce the alternative Reynolds and Strouhal numbers as $Re_d = U_\infty c \sin(\alpha) / \nu$ and $Re_h = U_\infty h / \nu$, and $St_d = f c \sin(\alpha) / U_\infty$ and $St_h = f h / U_\infty$. As shown in figure 11(b), d and h are rather different in the considered range of α . Interestingly, figure 11(c) shows that for modes pA and pB , $Re_{d,c1}$ collapses quite nicely to the same value for the different α , i.e. $Re_{d,c1} = 91.46 \pm 10.77$ for mode pA and $Re_{d,c1} = 105.91 \pm 18.67$ for mode pB ; its relative variation is much lower than that of Re_{c1} (compare figure 9). This shows that $d = c \sin(\alpha)$ is the appropriate length scale to describe the onset of the primary instability for negative α , and to predict whether the low- Re steady flow is absolutely and globally unstable to 2-D perturbations without the need of a stability analysis. In contrast, the same cannot be said for mode pC . In this case, indeed, at criticality, $Re_{d,c1}$ does not collapse to a same value for the different α considered. This is consistent with the fact that the triggering mechanism of mode pC is embedded in the fV_2 recirculating region at the TE and resembles what has been observed for 2-D symmetric bluff bodies (Chiarini *et al.* 2022b).

5. Intermediate Re : 2-D periodic flow

In §4, we have investigated the linear stability of the low- Re steady base flow and identified the eigenmodes that yield its primary bifurcation. To study the bifurcations the flow undergoes at larger Re , we (i) perform Floquet linear stability analysis of the ensuing limit cycles and (ii) use 2-D and 3-D direct numerical simulations to account for

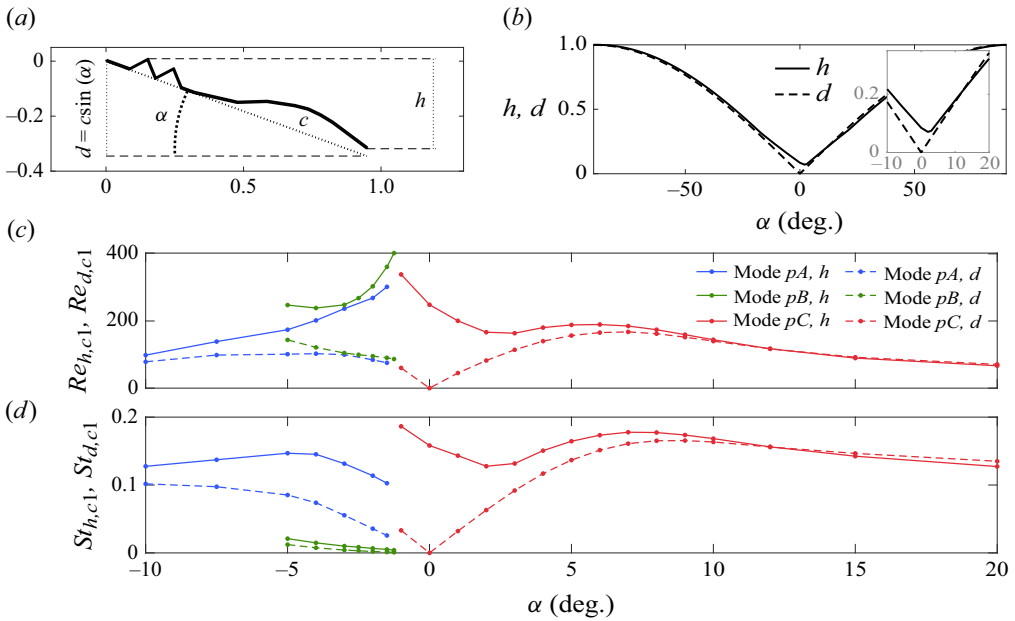


Figure 11. Neutral curves for modes pA , pB and pC , and corresponding frequency at criticality using alternative definitions of the Reynolds and Strouhal numbers, based on two different measures (d and h) of the vertical extent of the body. Panel (a) sketches how d and h are defined. Panel (b) shows the dependence of d and h on α . Panels (c) and (d) are as in figure 9, but for $Re_d = U_\infty d/\nu$, $St_d = f d/U_\infty$ and $Re_h = U_\infty h/\nu$, $St_h = f h/U_\infty$.

nonlinear effects. Depending on α , different limit cycles are possible, each one characterised by a different vortex interaction. Therefore, the nature of the secondary bifurcation changes with α . In this section, the different 2-D limit cycles are characterised, using $\alpha = -5^\circ, -1.5^\circ, 3^\circ, 7^\circ$ and 10° as representative cases.

5.1. Large negative angles of attack: $\alpha = -5^\circ$

We start examining large negative α . Figure 12 considers $\alpha = -5^\circ$ at $Re = 1490$, and plots four instantaneous snapshots taken equally spaced within the shedding period in panels (a)–(d). Note that this is the stabilised base flow (by means of the BoostConv algorithm), as the secondary bifurcation occurs at slightly smaller Re (see § 6.1). Streamlines and stagnation points are used to reveal the dynamics of the vortex shedding. As for smaller Re , several recirculating regions arise due to the presence of the sharp corners. The flow separates at the bottom LE corner but does not reattach, giving rise to a large recirculating region that encompasses the entire bottom side. For these values of α and Re , the flow unsteadiness is mainly driven by the dynamics of the recirculating regions placed in the rear part of the body. We focus first on the top side of the airfoil and consider the recirculating region that arises at the TE; see the $\Psi_2 = 0$ line separating from the body in panel (a). As time advances, this recirculating region enlarges and accumulates negative vorticity. Eventually, a hyperbolic stagnation point arises downstream the bottom TE corner (Boghossian & Cassel 2016), and the TE vortex with negative vorticity is shed in the wake (see panel b). The shedding of TE vortices with positive vorticity is related to the dynamics of the large recirculating region placed over the bottom side, close to the TE. Along the shedding period, it enlarges until it undergoes vortex splitting (see the

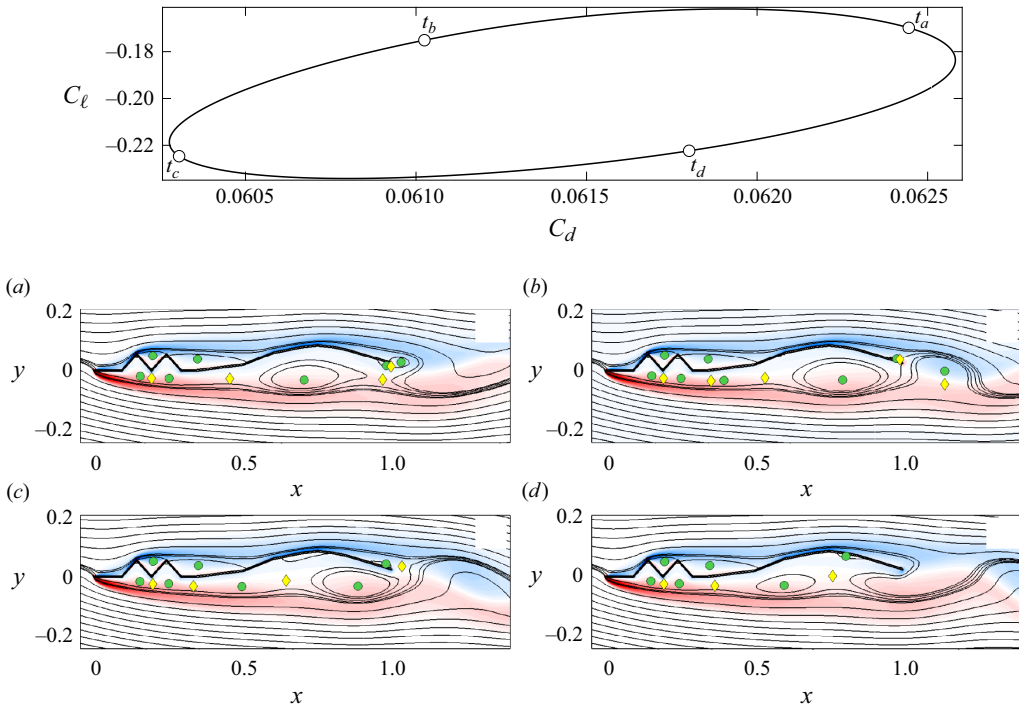


Figure 12. Instantaneous flow for $\alpha = -5^\circ$ at $Re = 1490$, represented with streamlines and vorticity colour maps. The periodic flow has period $T \approx 0.933$. (a–d) Four temporal instants are taken equally spaced in the shedding period. Green circles indicate elliptical stagnation points, whereas yellow diamonds indicate the hyperbolic stagnation points.

hyperbolic stagnation point in panels *d* and *a* below the TE) and a new TE vortex with positive vorticity is shed in the wake.

Note that for this α , the attractor draws a close line in the $C_l - C_d$ map that does not intersect itself: this indicates that the $C_l(t)$ and $C_d(t)$ signals are not in phase, and that the phase delay ϕ between them is in the $0 \leq \phi \leq \pi/2$ range.

5.2. Small negative angles of attack: $\alpha \leq -1.25^\circ$

For less negative α ($\alpha = -1.5^\circ$), the scenario changes; see [figure 13](#). After separating at the LE, the flow reattaches along the bottom side of the body, giving origin to a recirculating region that enlarges and shrinks, and periodically sheds vortices. This LE vortex shedding locks to the frequency of the vortex shedding from the TE, resembling what was found in the flow past 2-D elongated rectangular cylinders at intermediate Re (Okajima 1982; Hourigan, Thompson & Tan 2001); see also § 5.4. In contrast, the recirculating region that arises over the top side downstream of the corrugations does not play a central role in the dynamics of the wake for these α and Re ; it enlarges and shrinks, but does not undergo vortex splitting. We now focus on the bottom side, and start from panel (b). Advancing in time, the fore recirculating region progressively enlarges and eventually splits, shedding a LE vortex with positive vorticity. This is visualised in panels (c) and (d): as the reattaching point moves downstream, a new vortex arises, identified by the additional elliptic stagnation point that emerges in panel (c). The new LE vortex enlarges, until it is shed and travels downstream. When the LE vortex reaches the TE, it gives rise to a TE vortex with positive vorticity that is eventually shed in the wake. The shedding of

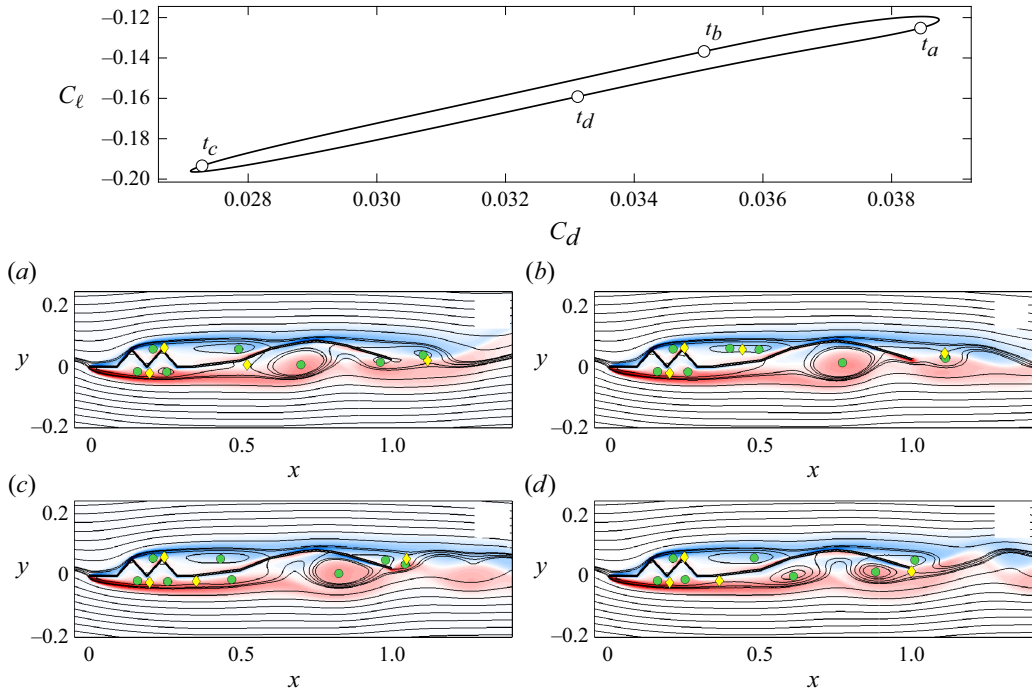


Figure 13. Instantaneous flow for $\alpha = -1.5^\circ$ at $Re = 3500$, represented with streamlines and vorticity colour maps. The periodic flow has period $T \approx 1.042$. (a)–(d) Four temporal instants are taken equally spaced in the shedding period. Green circles indicate elliptical stagnation points, whereas yellow diamonds indicate the hyperbolic stagnation points.

TE vortices with negative vorticity, instead, is related to the dynamics of the recirculating region that arises over the rear top side, and its frequency is dictated by the motion of the bottom LE vortex. In fact, a new TE vortex with negative vorticity is shed in the wake when the bottom LE vortex crosses the TE, and a new hyperbolic stagnation point arises there; see panels (d) and (a). Interestingly, this mechanism resembles what was observed by Chiarini *et al.* (2022b) for the flow past 2-D rectangular cylinders, in the regime dominated by the LE vortex shedding.

The shape of the $C_l - C_d$ curve differs from what we have found for $\alpha = -5^\circ$: in this case, indeed the two $C_l(t)$ and $C_d(t)$ signals are substantially in phase. We anticipate that a similar shape is also observed for larger α .

5.3. Small angles of attack: $-1.25^\circ < \alpha \leq 3^\circ$

We now move to small positive and negative α in the $-1.25^\circ < \alpha \leq 3^\circ$ range. Figure 14 considers $\alpha = 3^\circ$ at $Re = 5000$.

Over the top side, the flow separates at the corner of the upstream groove and reattaches along the rear arc, giving rise to two recirculating regions, separated by a hyperbolic stagnation point. However, they do not play a role in the vortex shedding mechanism. In fact, despite the presence of the hyperbolic stagnation point, the downstream recirculating region is not shed, as it instead occurs at larger α (see the following discussion). Moving downstream, the flow separates again due to the adverse pressure gradient, and a further recirculating region arises close to the TE (see panel a). As time advances, this recirculating region widens, until the reattaching point reaches the TE and a vortex with negative vorticity is shed in the wake (see panel b). Once this TE vortex is shed in the

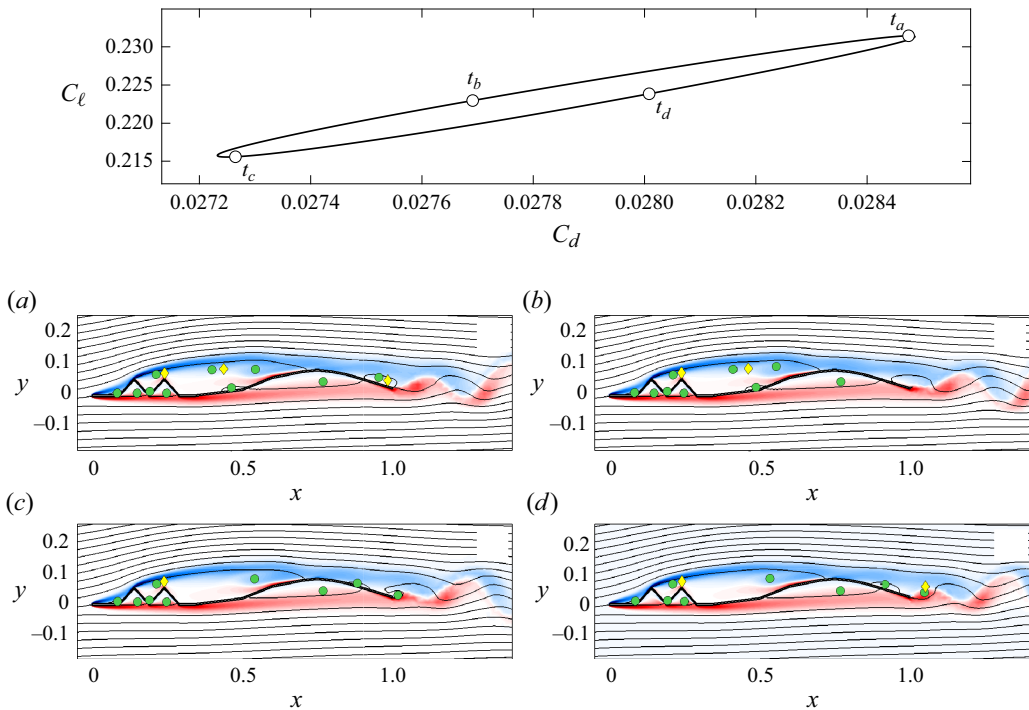


Figure 14. Instantaneous flow for $\alpha = 3^\circ$ at $Re = 5000$, represented with streamlines and vorticity colour maps. The periodic flow has period $T \approx 0.367$. (a)–(d) Four temporal instants are taken equally spaced in the shedding period. Green circles indicate elliptical stagnation points, whereas yellow diamonds indicate the hyperbolic stagnation points.

wake, a recirculating region with positive vorticity starts accumulating at the bottom TE corner (panel c), widens and, eventually, is shed in the wake (panel d).

5.4. Intermediate positive angles of attack: $4^\circ \leq \alpha \leq 7^\circ$

Figure 15 considers $\alpha = 7^\circ$ at $Re = 4700$, being representative of α in the $4^\circ \leq \alpha \leq 7^\circ$ range. Unlike for smaller α , here, the recirculating region that arises after the flow separation at the upstream groove corner plays a role in the vortex shedding dynamics. This recirculating region periodically splits, releasing vortices that are advected downstream and give rise to TE vortices. This resembles the periodic vortex shedding observed in the flow past elongated rectangular cylinders, with $\mathcal{R} = L/D > 3$ (here, L and D are the streamwise and vertical sizes of the cylinder). In that case, indeed, due to the so-called impinging leading-edge vortex (ILEV) instability, vortices are periodically shed from the LE and TE shear layers, and the two phenomena lock to the same frequency (Okajima 1982; Nakamura & Nakashima 1986; Mills *et al.* 1995; Hourigan *et al.* 2001; Chiarini *et al.* 2022b). The mechanism of the ILEV instability is the following. A vortex is shed from the LE shear layer and is advected downstream. When the LE vortex passes over the TE, it creates a perturbation that alters the flow circulation and triggers thus the shedding of a new LE vortex. At the same time, the interaction of the LE vortex with the TE induces vortex shedding in the wake. The vortex dynamics of the limit cycle at these intermediate α is similar. We consider the top side of the body, and start from figure 15(c). Within the $\Psi_2 = 0$ line that separates at the upstream groove corner, three recirculating regions are detected, being separated by hyperbolic stagnation points. As time advances,

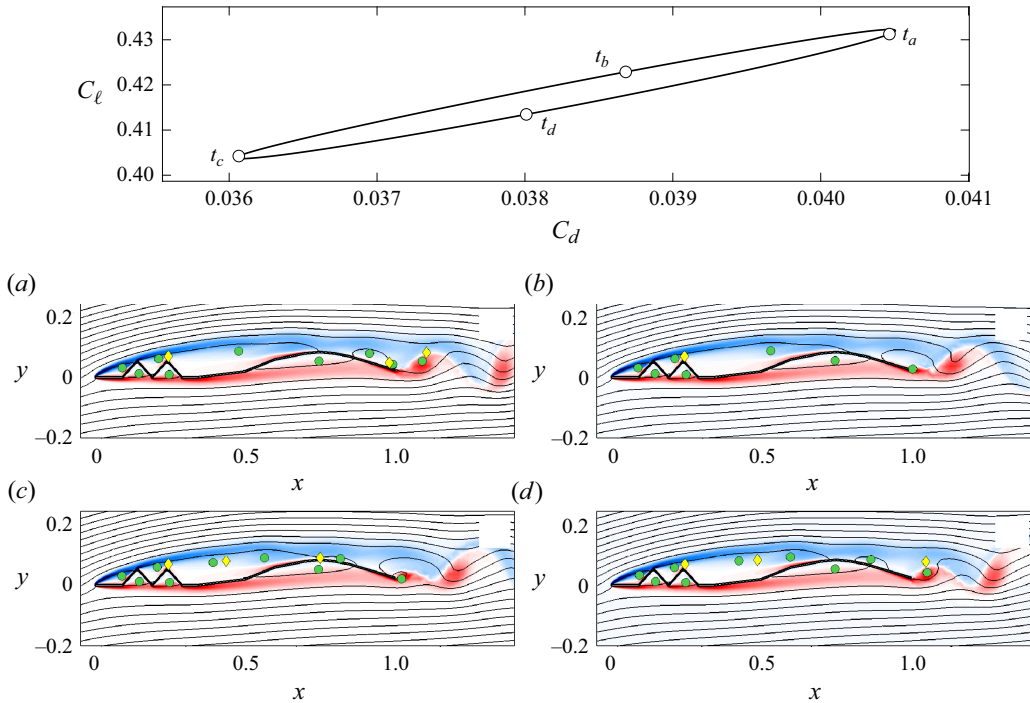


Figure 15. Instantaneous flow for $\alpha = 7^\circ$ at $Re = 4700$, represented with streamlines and vorticity colour maps. The periodic flow has period $T \approx 0.419$. (a)–(d) Four temporal instants are taken equally spaced in the shedding period. Green circles indicate elliptical stagnation points, whereas yellow diamonds indicate the hyperbolic stagnation points.

the recirculating region widens and then shrinks, splitting into two parts: an LE vortex is shed (panel *c*) and travels downstream (panel *d*). When the LE vortex reaches the TE (panel *a*), a hyperbolic stagnation point arises at the bottom side and a new TE vortex with negative vorticity is shed in the wake (panel *b*). At the same time, a recirculating region with positive vorticity starts accumulating at the bottom TE corner (panels *b* and *c*), being eventually shed in the wake a half-period later (panel *d*). More specifically, the vortex dynamics over the top side of the geometry closely resembles the flow past rectangular cylinders in the case where the preferred TE shedding frequency is permitted (Chiarini *et al.* 2022*b*).

5.5. Large positive α

We now move to $\alpha \geq 8^\circ$ and use $\alpha = 10^\circ$ at $Re = 2000$ as a representative case; see figure 16. For these values of α and Re , the flow separates at the corner of the upstream corrugation and only intermittently reattaches on the top body surface. We start from panel (a). Here, the flow reattaches at $x \approx 1$ and an elliptic stagnation point detects a recirculating region close to the TE. As time advances, the flow separates and a TE vortex with negative vorticity is shed in the wake (panel *b*). At the same time, a recirculating region with positive vorticity starts accumulating at the bottom TE corner (panel *b*), it widens (panel *c*) and, eventually, it is shed in the wake (panel *d*). When this shedding occurs, the flow reattaches over the rear top side and a new recirculating region with negative vorticity forms close to the TE.

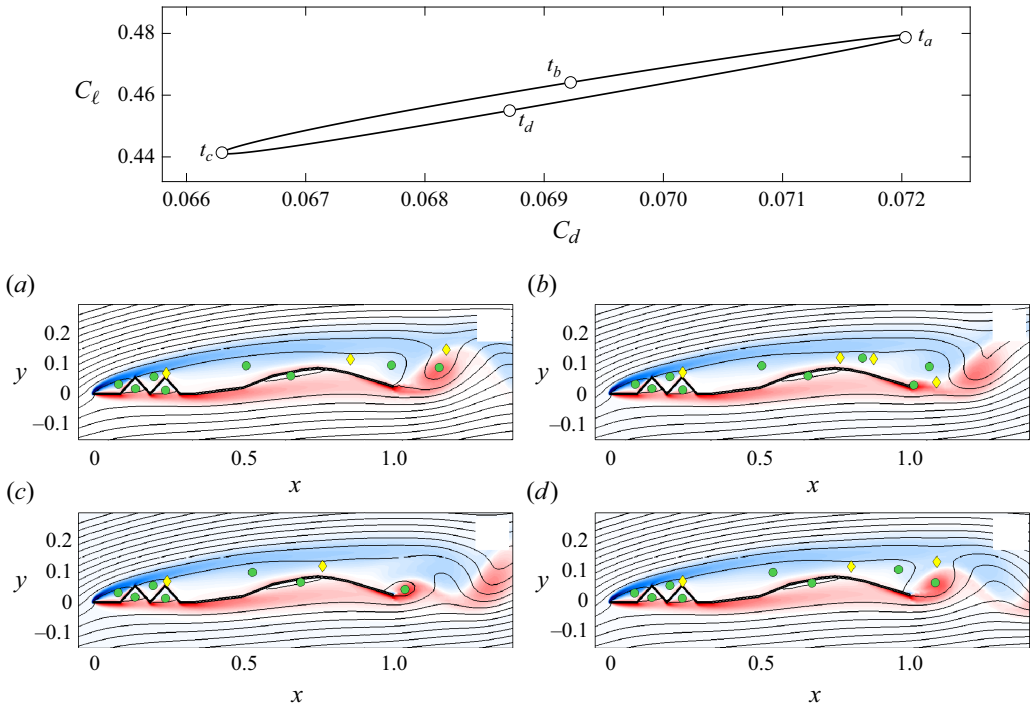


Figure 16. Instantaneous flow for $\alpha = 10^\circ$ at $Re = 2000$, represented with streamlines and vorticity colour maps. The periodic flow has period $T \approx 0.691$. (a)–(d) Four temporal instants are taken equally spaced in the shedding period. Green circles indicate elliptical stagnation points, whereas yellow diamonds indicate the hyperbolic stagnation points.

6. Secondary bifurcation

Having characterised the periodic limit cycles at intermediate Re , we now address the secondary bifurcation of the flow by means of Floquet analysis. Both 2-D and 3-D nonlinear simulations are used to corroborate the results. For negative α , the secondary instability is 2-D. To reiterate (see figure 3), for intermediate negative α , the secondary flow instability consists of a 2-D Neimark–Sacker bifurcation and introduces a new frequency that matches that of mode pB described in § 4. For large negative α , instead, the secondary instability consists of a 2-D subharmonic bifurcation and leads to a new limit cycle. For positive α , the secondary bifurcation is 3-D. Different growing modes are detected with the Floquet analysis. For $0^\circ \leq \alpha \leq 7^\circ$, the leading mode is synchronous and the secondary instability yields a 3-D pitchfork bifurcation. For larger α , instead, the most amplified mode is of subharmonic nature.

6.1. 2-D secondary bifurcation for $-5^\circ \leq \alpha \leq -1.5^\circ$

We start considering small negative α , using $\alpha = -1.5^\circ$ as a representative case. As anticipated, for $-5^\circ < \alpha \leq -1.25^\circ$, the limit cycle loses its stability at $Re = Re_{c2}$ by means of a 2-D Neimark–Sacker bifurcation. For $Re \geq Re_{c2}$ ($Re_{c2} \approx 3568$ for $\alpha = -1.5^\circ$), the nonlinear simulations reveal that a new frequency incommensurate with that of the limit cycle emerges in the spectrum and a torus replaces the limit cycle in the phase space. Notably, the new frequency matches reasonably well that of the unsteady mode pB of the low- Re steady base flow. For $\alpha = -1.5^\circ$ and $Re = 3750$, for example, from the nonlinear simulations, we measure $St \approx 0.05$, which has to be compared with the value of

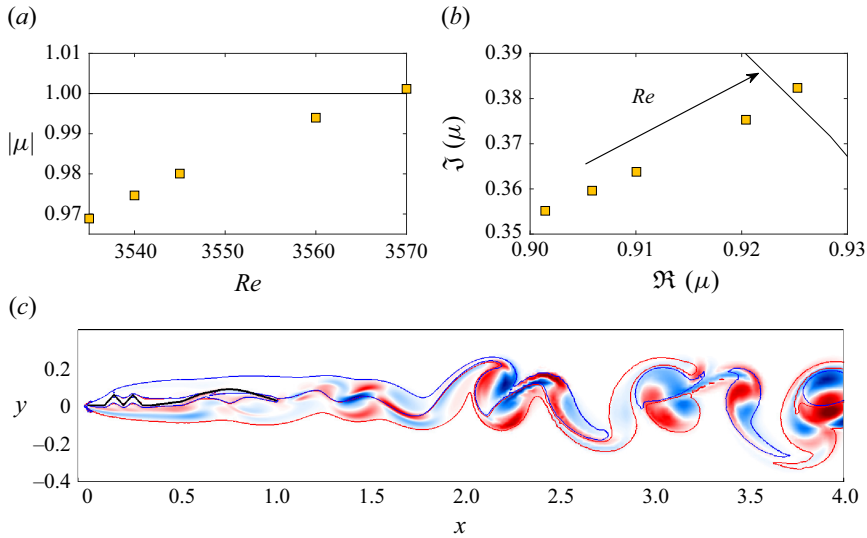


Figure 17. Secondary bifurcation for $\alpha = -1.5^\circ$. (a),(b) Dependence of the leading branch of Floquet multipliers on Re : (a) dependence of $|\mu|$ on Re ; (b) Floquet multipliers in the complex plane; the arrow indicate the direction increase of Re . (c) Floquet mode responsible for the secondary bifurcation at $Re = 3500$. The colourmap represents contours of spanwise vorticity of the perturbation field, while the red and blue solid lines are isocontours $\Omega_{z,2} = \pm 0.5$ of the periodic base flow.

$f_{c1} \approx 0.046$ found for mode pB at criticality with the linear stability analysis (figure 9). It is also worth noticing that the value of Re_{c2} is very close to the critical Reynolds number found for pB , which for $\alpha = -1.5^\circ$ is $Re \approx 3475$.

To further characterise this bifurcation, we have investigated the linear stability of the limit cycle via Floquet analysis. The results are shown in figure 17: panels (a) and (b) highlight the dependence of the Floquet multipliers on Re , while panel (c) depicts the spatial structure of the unstable Floquet mode. A leading branch of multipliers with $\beta = 0$ has been detected. It corresponds to a pair of complex conjugate multipliers that near the unit cycle as Re increases, with positive real part and non-null imaginary part, in agreement with a 2-D secondary Hopf bifurcation. We refer to this mode as mode $sQPb$. At $Re = 3570$, the multipliers are $\mu = (0.926 \pm 0.382i)$, which correspond to Floquet exponents of $\sigma_2 = (0.0011, \pm 0.3737i)$ and therefore to a frequency of $f \approx 0.0595$ that is close to the results of the nonlinear simulations. Note that in agreement with mode pB of the low- Re steady base flow, the magnitude of mode $sQPb$ is non-null along the bottom side of the airfoil; see figure 17(c).

For large negative α , the scenario is more convoluted. This is visualised in figure 18 by means of the results of the 3-D nonlinear simulations for $\alpha = -5^\circ$. We find that at $Re = 1200$, the flow is periodic and the flow dynamics is driven by mode pA of the low- Re steady base flow. When increasing Re up to $Re = 1450$, an additional peak at a frequency that matches that of pB arises in the frequency spectrum, but only in the initial transient; see figure 18(a). For long integration times, indeed, the peak disappears, the corresponding flow oscillations are attenuated and the flow recovers its 2-D periodic behaviour ($St \approx 1.06$). At $Re = 2000$, instead, the nonlinear simulations show that the flow remains 2-D, but settles into a limit cycle with a frequency of $St \approx 0.56$ which is half that of the original one; see figure 18(b). For large negative α , the secondary bifurcation is thus 2-D and subharmonic.

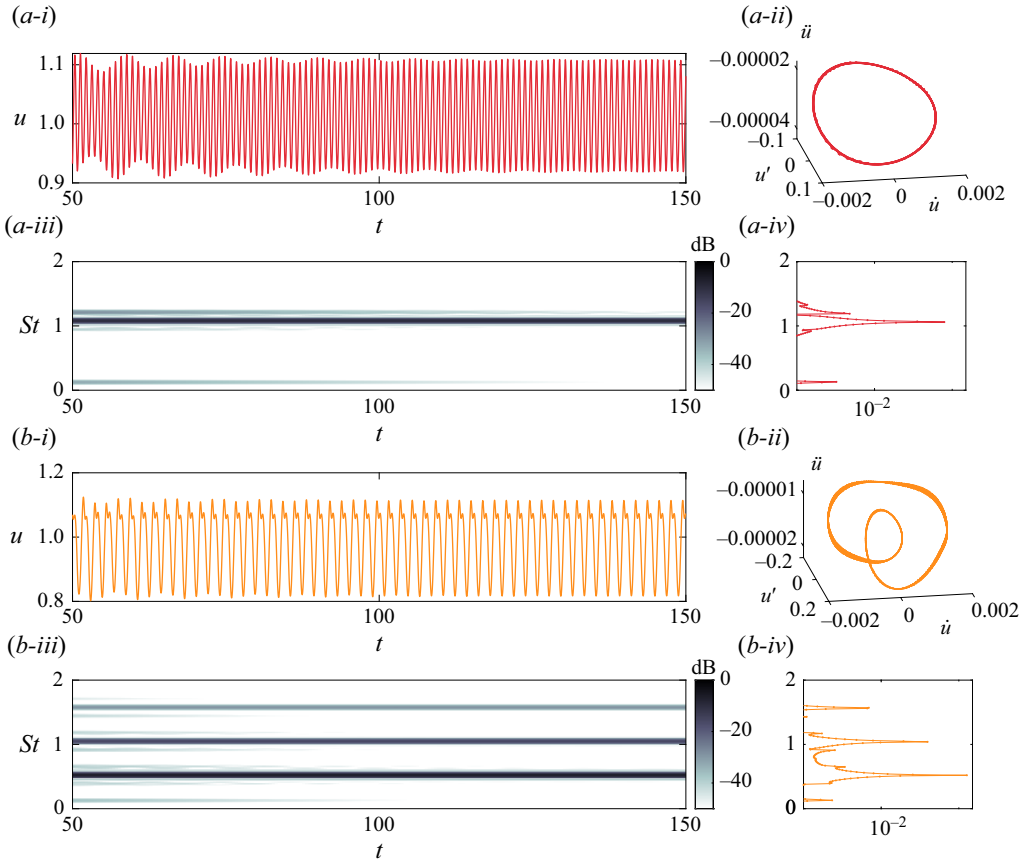


Figure 18. Results from DNS at $\alpha = -5^\circ$ for (a) $Re = 1450$ and (b) $Re = 2000$: (i) streamwise velocity signal u at $(x, y, z) = (1.3, 0.17, 0.5)$; (ii) flow attractor for $t > 150$; (iii) sliding FFT; (iv) FFT corresponding to the streamwise velocity signal figure in panel (i).

The Floquet analysis supports this picture. In fact, as shown in figure 19, for $\alpha = -5^\circ$, mode $sQPb$ does not exhibit a positive amplification rate (i.e. $|\mu| < 1$) in the range of Re investigated. The modulus of the corresponding Floquet multipliers first increases with Re , with the multiplier almost crossing the unit circle for $Re = 1350$ (i.e. $|\mu| \approx 1$) and then decays for larger Re . For $Re = 1350$, the pair of complex conjugate multipliers is $\mu = (0.755, \pm 0.654)$, corresponding to Floquet exponents of $\sigma_2 = (-0.0011, \pm 0.7606)$ and to a frequency of $f \approx 0.12$, which is very close to the $St \approx 0.13$ value detected in the transient of the nonlinear simulation and found for mode pB at criticality. Note that unlike for $\alpha = -1.5^\circ$, for $\alpha = -5^\circ$, mode $sQPb$ exhibits a quasi-zero growth rate (marginal stability) at a Reynolds number that is smaller than the $Re_{c,pB} \approx 1650$ found with the stability analysis of the low- Re steady base flow. In agreement with the nonlinear simulations, the Floquet analysis detects an additional branch of multipliers with $\beta = 0$ that indeed becomes amplified at $Re \gtrsim 1480$. For $Re < 1470$, this branch consists of a pair of complex conjugate multipliers with negative real part and a non-null imaginary part that decreases as Re increases. At $Re \approx 1470$, the two multipliers collapse on the real axis and become real. Then, further increasing Re , the two multipliers move along the real axes and one crosses the unit circumference at $Re \approx 1480$ and the corresponding mode exhibits a positive growth rate: this confirms that the secondary bifurcation of the flow is 2-D and

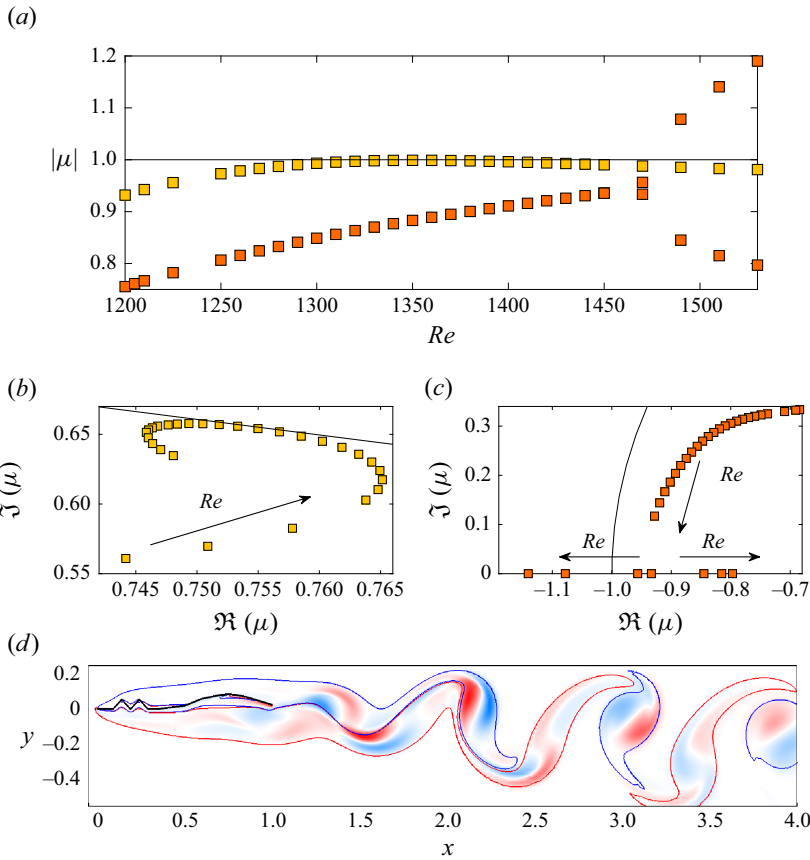


Figure 19. Secondary bifurcation for $\alpha = -5^\circ$: (a) dependence of the modulus of the Floquet multipliers on Re ; (b) Floquet multipliers associated with the mode $sQPb$ in the complex plane; (c) Floquet multipliers associated with the mode sSb responsible for the secondary bifurcation; (d) Floquet mode responsible for the secondary bifurcation at $Re = 1510$. The colourmap represents contours of spanwise vorticity of the perturbation field, while the red and blue solid lines are isocontours $\Omega_{z,2} = \pm 0.5$ of the periodic base flow.

of subharmonic nature. Figure 19 shows the structure of the Floquet mode responsible for the bifurcation, referred to as mode sSb . Similarly to mode $sQPb$, this mode has large values in the wake and over the bottom side of the body. In the wake, the perturbation field synchronises with the base flow, with perturbation dipoles being placed within the base flow monopoles. The orientation of these dipoles changes from one period to the next one accordingly with the subharmonic nature of the mode.

6.2. 3-D synchronous bifurcation for $-1.25^\circ < \alpha \leq 7^\circ$

For $-1.25^\circ < \alpha \leq 7^\circ$, the secondary bifurcation leads to a 3-D flow that preserves the same temporal periodicity of the periodic base flow; see figure 3. In this section, we detail this bifurcation by considering $\alpha = 3^\circ$ and $\alpha = 7^\circ$ as representative cases. We only investigate the leading modes of the periodic limit cycles, i.e. those that drive the secondary instability of the flow.

For all α in the $-1.25^\circ < \alpha \leq 7^\circ$ range, the secondary instability consists of a pitchfork bifurcation that leads to a 3-D state with the same periodicity of the non-bifurcated 2-D limit cycle. Like the well-known cases of the circular and square cylinders (Barkley &

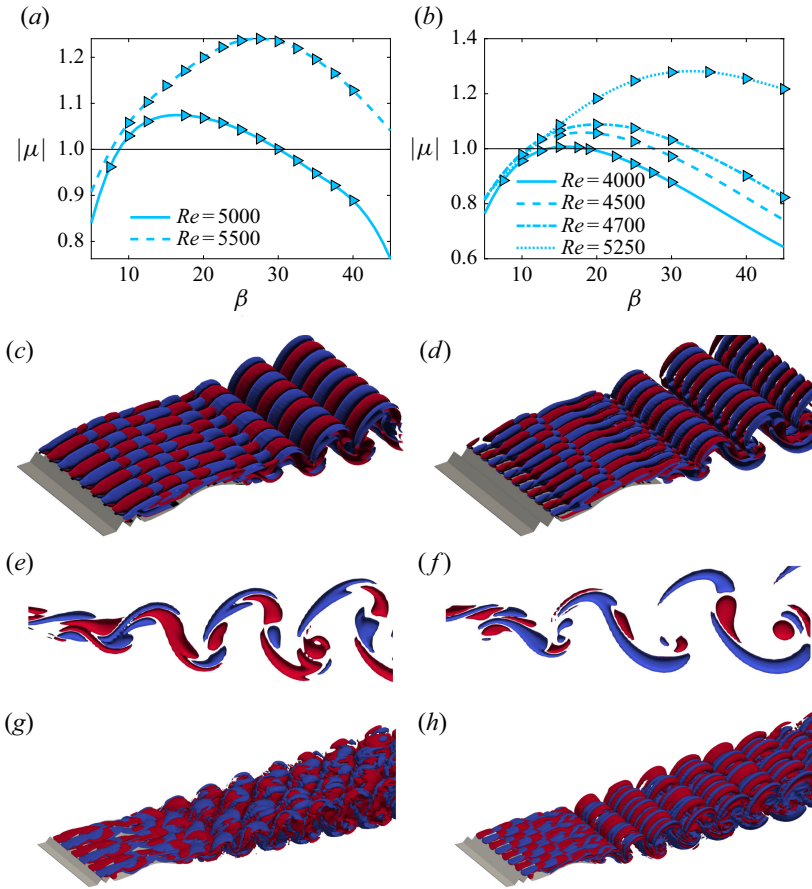


Figure 20. Secondary bifurcation for (a,c,e,g) $\alpha = 3^\circ$ and (b,d,f,h) $\alpha = 7^\circ$ via mode sA . (a, b) Modulus of the Floquet multipliers associated with the most amplified mode as a function of β and Re . Here, all the multipliers are real and positive. (c, d) Three-dimensional reconstruction of the Floquet mode over a spanwise extent of $L_z = c$ for (c) $\alpha = 3^\circ$, $Re = 5500$ and $\beta = 25$ and (d) $\alpha = 7^\circ$, $Re = 5250$ and $\beta = 35$. The red/blue colour denotes positive/negative isosurfaces of the streamwise vorticity with value $\hat{\omega}_{x,2} = \pm 5$. (e, f) Lateral view and a zoom-in on the wake region of panels (c, d). (g, h) Instantaneous snapshot from the nonlinear 3-D simulations for (g) $\alpha = 3^\circ$ and $Re = 5500$ and (h) $\alpha = 7^\circ$ and $Re = 5250$. The red/blue colour denotes positive/negative (total) streamwise vorticity with value $\omega_x = \pm 0.5$.

Henderson 1996; Robichaux *et al.* 1999), the 2-D periodic flow is linearly unstable to synchronous 3-D perturbations. Figure 20 characterises the bifurcation for $\alpha = 3^\circ$ (panels a,c,e,g) and $\alpha = 7^\circ$ (panels b,d,f,h) using results from Floquet stability analysis (panels a–f) and the 3-D nonlinear simulations (panels g,h). For all cases, the Floquet analysis shows that the first multiplier to cross the unit circle is real and positive. The critical Reynolds number $Re_{c,2}$ decreases with α , being slightly less than $Re = 5000$ for $\alpha = 3^\circ$ and $Re_{c,2} \approx 4500$ for $\alpha = 7^\circ$, in agreement with the results of the nonlinear simulations shown in figure 3. For $Re > Re_{c,2}$, a band of amplified wavenumbers appears and widens as Re increases, with the leading branch moving towards larger β ; see figure 20(a, b). The critical wavenumber is $\beta_c \approx 15–20$ at $Re \approx Re_{c,2}$, and slightly increases with α . Hereafter, we refer to this mode as mode sA . Notably, this perfectly matches with the results of the 3-D nonlinear simulations; see figure 20(g, h). Indeed, the wavenumbers emerging after the establishment of the secondary mode are $\beta = 2\pi/\lambda_z \approx 19$

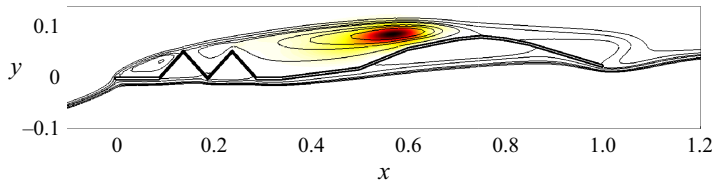


Figure 21. Time averaged structural sensitivity for mode sA for $\alpha = 7^\circ$, $Re = 5250$ and $\beta = 35$.

for $\alpha = 3^\circ$ and $Re = 5500$, and $\beta = 2\pi/\lambda_z \approx 25$ for $\alpha = 7^\circ$ and $Re = 5250$; note that at these Re , the flow is already the non-periodic regime for both α (see figure 3). The small discrepancy with the β_c values detected with the stability analysis is due to the considered Re that is above the Re_{c2} threshold and to the periodic boundary conditions that enforce the wavelength of the disturbance to be a sub-multiplier of ℓ_z .

Overall, these results show that the route to three-dimensionalisation for non-smooth airfoils differs from what is found for smooth airfoils. Indeed, in the present case, due to the complex vortex interaction on the top side of the airfoil (see the following discussion), the flow three-dimensionalisation is driven by the synchronous mode sA , while Gupta *et al.* (2023) found that for NACA airfoils, the first 3-D mode to become amplified is of subharmonic nature for all α .

The central panels of figure 20 show the spatial structure of mode sA (reconstructed in the spanwise direction in the range of $0 \leq z \leq 1$) for $\alpha = 3^\circ$ (panels c and e) and $\alpha = 7^\circ$ (panels d and f). The perturbation fields are maximum near the vortex cores of the base flow, as typical for the flow past bluff bodies (see for example Thompson, Leweke & Williamson 2001). Unlike for short bluff bodies (Barkley & Henderson 1996; Robichaux *et al.* 1999; Choi & Yang 2014) or for elongated bluff bodies with streamlined LE (Ryan *et al.* 2005), here, the perturbations are not localised in the wake, but large values are detected also over the top side of the body. The same structure is observed also with the 3-D nonlinear simulations (panels g and h). This recalls the mode QS of the flow past elongated rectangular cylinders (Chiarini *et al.* 2022a) and indicates that this is not a growing mode of the wake, but it is related to the dynamics of the vortices over the lateral side of the airfoil, as shown in the following with the structural sensitivity. Note that the symmetry is such that the sign of the streamwise vorticity does not change from one period to the next, in agreement with the synchronous nature of the mode. The spatial structure of mode sA changes when α increases, in agreement with the change of the base flow; see figure 20(e, f). Unlike for larger α ($\alpha = 7^\circ$), for small α ($\alpha = 3^\circ$), the streamwise vorticity in the braid regions that connect the vortex cores changes sign from one half-period to the next one.

Figure 21 shows the spectral norm of the time-averaged structural sensitivity tensor (Giannetti, Camarri & Luchini 2010)

$$S(x, y, \beta) = \frac{\int_t^{t+T} \hat{\mathbf{u}}^\dagger(x, y, \beta, t) \hat{\mathbf{u}}(x, y, \beta, t) dt}{\int_t^{t+T} \int_\Omega \hat{\mathbf{u}}^\dagger \cdot \hat{\mathbf{u}} d\Omega dt} \quad (6.1)$$

for mode sA . Here, we consider $\alpha = 7^\circ$, but the same distribution has been found also for smaller α . The norm $\|S\|$ of the sensitivity tensor vanishes almost everywhere, except near the top side of the body, indicating a localised wavemaker region. In agreement with the spatial structure of the direct modes, this differs from what is observed for the classical modes A and B of the circular cylinder case, as the structural sensitivity does not peak in the wake region, but within the recirculating regions that arises downstream of the two grooves. This confirms that the triggering mechanism is localised in this region and is

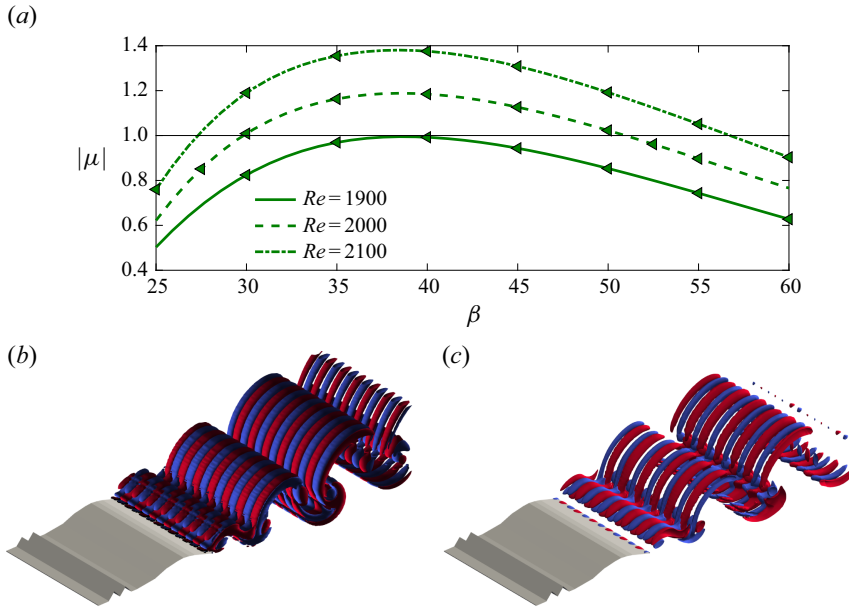


Figure 22. Secondary bifurcation for $\alpha = 10^\circ$ via mode sS . (a) Modulus of the Floquet multipliers associated with the most amplified mode as a function of β and Re . Here, all the multipliers are real and negative. (b) Three-dimensional reconstruction of the Floquet mode for $Re = 2100$ and $\beta = 40$. The red/blue colour denotes positive/negative isosurfaces of the streamwise vorticity with value $\hat{\omega}_{x,2} \pm 5$. (c) Instantaneous snapshot from the nonlinear 3-D simulations at $Re = 2100$. The red/blue colour denotes positive/negative (total) streamwise vorticity with value $\omega_x \pm 2$.

related to the dynamics of the top side recirculating region. Despite the different vortex dynamics in the base flow, the map of $\|S\|$ has a similar spatial distribution for both small ($-1.25^\circ \leq \alpha \leq 3^\circ$) and intermediate ($4^\circ \leq \alpha \leq 7^\circ$) α , indicating that the vortex shedding over the lateral top side of the body observed for the latter (see § 5.4) does not play any role in the triggering mechanism. In particular, $\|S\|$ peaks close to the elliptic stagnation point that identifies the downstream recirculating region within the average $\Psi_2 = 0$ streamline that separates from the corrugations.

6.3. 3-D subharmonic bifurcation for $8^\circ \leq \alpha \leq 10^\circ$

We now focus on large positive α . For $8^\circ \leq \alpha \leq 10^\circ$, we find that the secondary flow instability consists of a 3-D subharmonic bifurcation (see figure 6). Here, we characterise this bifurcation and use $\alpha = 10^\circ$ as a representative case; see figure 22. Like in the previous section, we use both Floquet stability analysis (panels *a* and *b*) and 3-D nonlinear simulations (panel *c*).

The Floquet stability analysis reveals the existence of a growing multiplier crossing the unit circle at $\mu = (-1, 0)$ for $Re = Re_{c2} \approx 1900$, which is consistent with a subharmonic bifurcation; see figure 22(a). Hereafter, we refer to the corresponding mode as sS . The first multiplier with $|\mu| > 1$ appears at $\beta \approx 37.5$, denoting a wavelength of $\lambda_z = 2\pi/\beta \approx 0.175$, which is smaller with respect to that of mode sA . As Re increases, a band of amplified wavenumbers appears, with β_{max} however only marginally changing with Re .

The subharmonic nature of mode sS is conveniently visualised in figure 22(b), where the 3-D spatial structure of the Floquet mode is reconstructed: the sign of $\hat{\omega}_{x,2}$ changes from one period to the next one (see the alternate red/blue isosurfaces in the wake along

the streamwise direction). Notably, [figure 22\(b\)](#) also shows that, unlike sA , mode sS is a wake mode: in this case, the recirculating regions that arise over the top side of the airfoil do not play a role in the triggering mechanism. This scenario is corroborated by the 3-D nonlinear simulations. The instantaneous streamwise vorticity field in [figure 22\(c\)](#), indeed, shows that the 3-D perturbations grow downstream of the body in the near wake, exhibiting a wavenumber of $\beta = 12\pi \approx 37.7$, which is in perfect agreement with that provided by the Floquet analysis.

Similarly to what is found for the primary bifurcation and for mode sA , the critical Reynolds number Re_{c2} of mode sS decreases with α . According to the Floquet stability analysis, indeed, $Re_{c2} \approx 3200$ for $\alpha = 8^\circ$, $Re_{c2} \approx 2400$ for $\alpha = 9^\circ$ and $Re_{c2} \approx 1900$ for $\alpha = 10^\circ$ (not shown). Interestingly, the secondary instability for these large α agrees with the results of [Yang et al. \(2013\)](#) for inclined flat plates at $20^\circ \leq \alpha \leq 30^\circ$, and with those of [Gupta et al. \(2023\)](#) for a smooth NACA0012 airfoil. [Gupta et al. \(2023\)](#) indeed showed that for smooth airfoils, the flow three-dimensionalisation at these α ($9^\circ \lesssim \alpha \lesssim 10^\circ$) is driven by a subharmonic mode of the wake with spanwise wavelength of $\lambda_z \approx 0.2$, that is close to our findings.

7. Aerodynamic performance

Variations in the flow regime evidently affect the aerodynamic forces of the dragonfly-inspired geometry. [Levy & Seifert \(2009\)](#) showed that the corrugated airfoil shows superior performance compared with other smooth airfoils (for example, the low- Re Eppler-E61 airfoil). In particular, they found that despite the lifting capabilities of the dragonfly-inspired airfoil are generally lower, the large decrease of the mean drag coefficient leads to an enhanced aerodynamic efficiency at all α ; for additional details, we refer to [Appendix A](#), where the comparison is replicated for validation purposes. In this section, we discuss the aerodynamic performances of the corrugated airfoil in the considered portion of the $\alpha-Re$ parameter space and relate them to the detected flow regimes.

[Figure 23\(a-d\)](#) depicts the mean lift and drag coefficients as a function of α and Re . The mean lift-to-drag ratio $\overline{C_\ell/C_d}$ in the whole $\alpha-Re$ parameter space is also shown in [figure 23\(e\)](#); here and hereafter, the $\bar{\cdot}$ operator indicates time average. The symbols are the same as in [figure 3](#) and are used to highlight the flow regimes. As shown in [figure 23\(a\)](#), the mean lift coefficient $\overline{C_\ell}$ shows a trend similar to that of traditional airfoils. It increases until reaching the stall which occurs at $\alpha \approx 12^\circ$ for $Re = 3000$ and $\alpha \approx 10^\circ$ for $Re = 6000$. Therefore, in the considered range of Re , stall incidence decreases with the Reynolds number. Interestingly, the strong increase of $\overline{C_\ell}$ before the stall at $Re = 3000$ occurs immediately after the secondary 3-D bifurcation of subharmonic nature. The mean drag coefficient, instead, has a non-monotonic dependence on α for all Re , and shows the classical parabolic shape for $Re \lesssim 2000$ only; [figure 23\(b\)](#). An increase of Re leads to a growth of the scale selectivity ([Nastro, Fontane & Joly 2020](#)) and therefore to an increase of the flow sensitivity to the strongly-asymmetrical corrugated geometry. As a consequence, the $\overline{C_\ell}-\alpha$ and $\overline{C_d}-\alpha$ curves exhibit an accentuation of their asymmetry for increasing Re .

[Figure 23\(b, d\)](#) offers a complementary picture, with the $\overline{C_\ell}$ and $\overline{C_d}$ shown as a function of Re for fixed values of α . For $\alpha \leq 0^\circ$, when fixing α , $\overline{C_\ell}$ has a non-monotonic dependence on Re . For $\alpha > 0^\circ$, instead, $\overline{C_\ell}$ increases with Re , albeit for $\alpha \geq 9^\circ$, it stops growing at $Re \gtrsim 4000$. When fixing α , the mean drag coefficient has a non-monotonic dependence on Re for $\alpha > 7^\circ$: $\overline{C_d}$ decreases for small Re and then increases reaching a plateau for the largest Re . In this range, the minimum $\overline{C_d}$ increases with α and moves

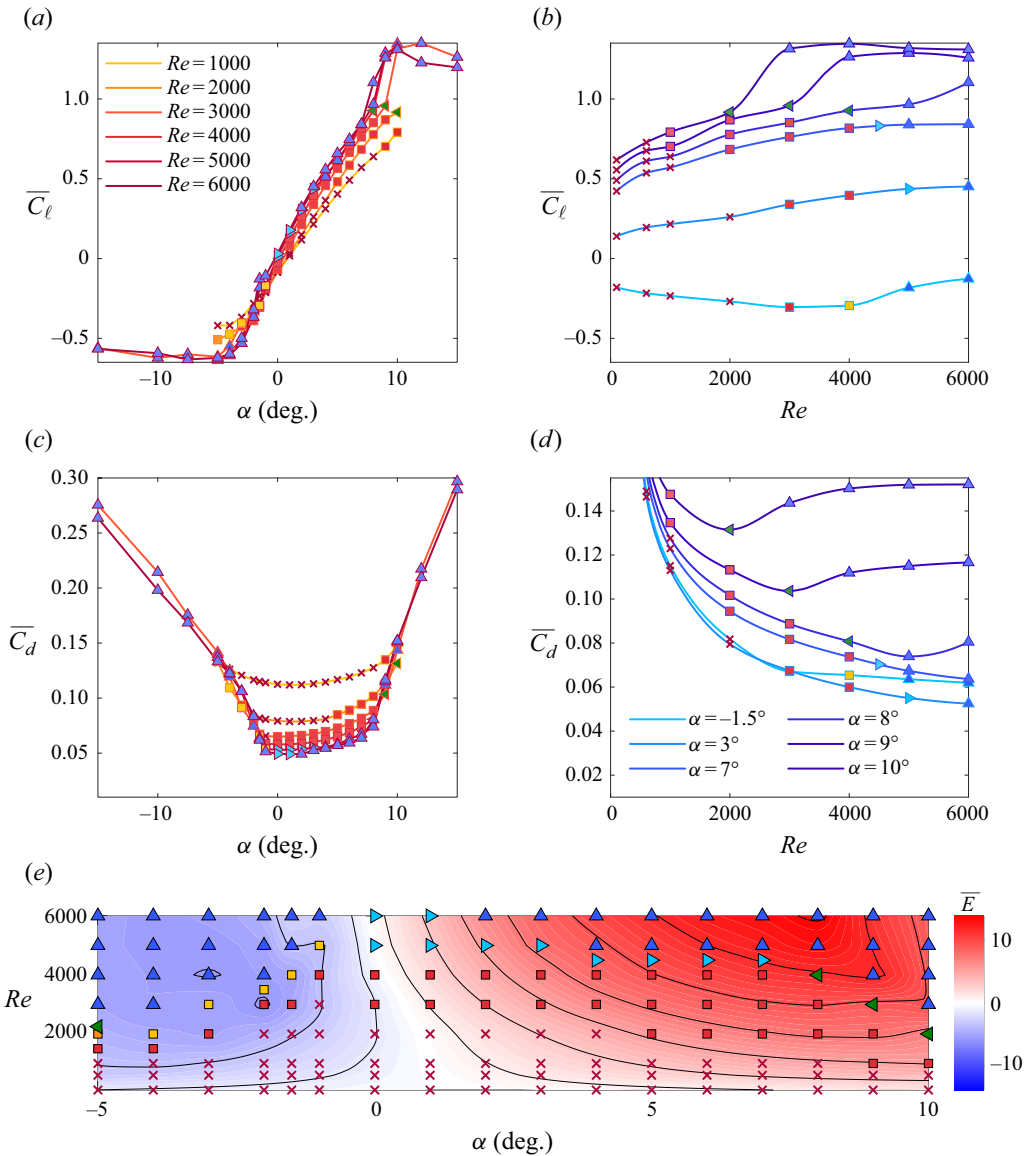


Figure 23. Mean aerodynamic forces: (a,b) mean lift coefficient as a function of (a) α and (b) Re ; (c,d) mean drag coefficient as a function of (c) α and (d) Re ; (e) mean lift-to-drag ratio in the $\alpha-Re$ parameter space. Symbols as in figure 3.

towards smaller Re . Interestingly, this minimum value corresponds, or is very close, to the 3-D subharmonic bifurcation of the limit cycle, i.e. $Re \approx 4000$ for $\alpha = 8^\circ$, $Re \approx 3000$ for $\alpha = 9^\circ$ and $Re \approx 2000$ for $\alpha = 10^\circ$ (see the green triangles). However, for $\alpha \leq 7^\circ$, \overline{C}_d monotonically decreases with Re in the considered range of parameters. For $0^\circ \leq \alpha \leq 7^\circ$, the secondary 3-D bifurcation via the synchronous mode (see the light blue triangles) does not induce a change in the trend of time-averaged aerodynamic coefficients when Re is increased.

As shown in figure 23(e), the combined effect of Re on \overline{C}_l and \overline{C}_d leads to a monotonic increase (decrease) of the aerodynamic efficiency with Re for $\alpha \geq -1^\circ$ ($\alpha \leq -1.5^\circ$).

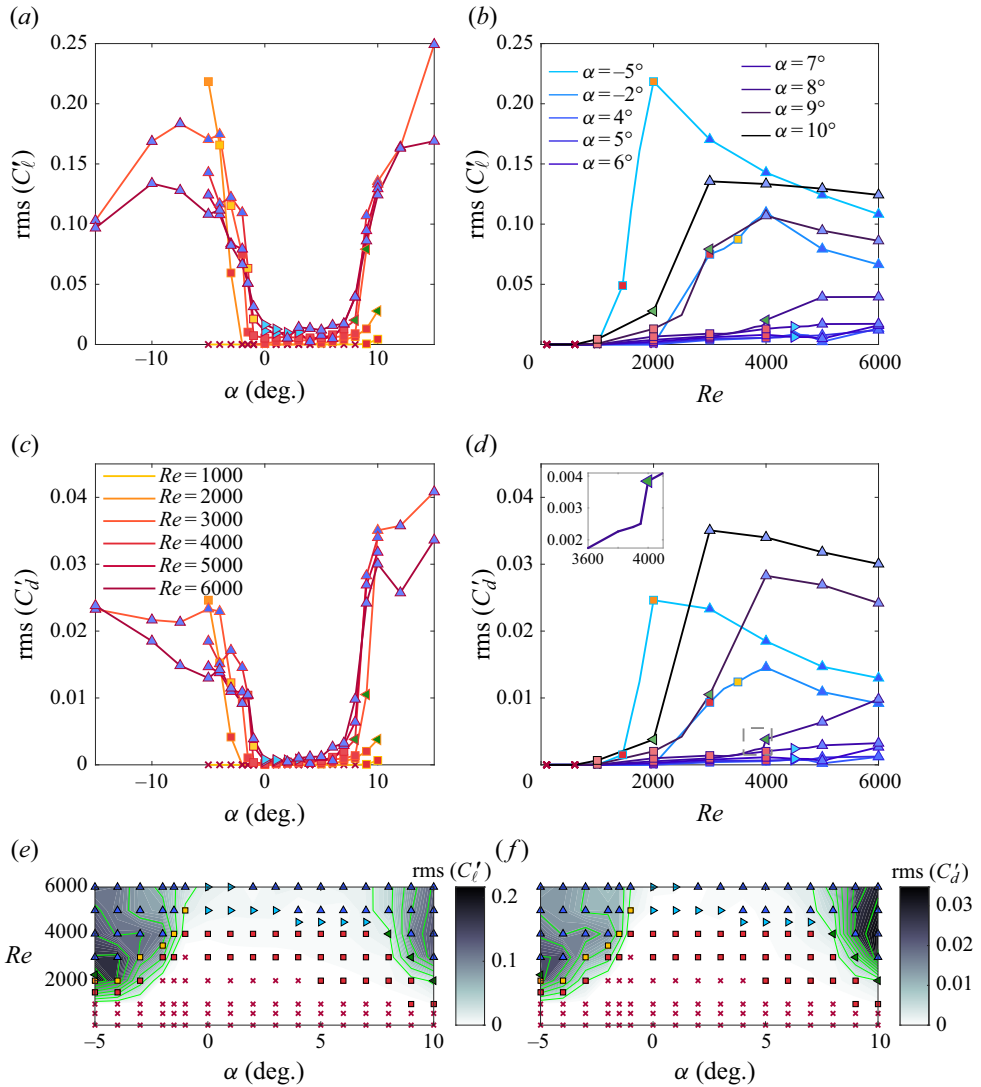


Figure 24. Root mean square of the aerodynamics forces: (a,b) lift coefficient root mean square (r.m.s.) as a function of (a) α and (b) Re ; (c,d) drag coefficient r.m.s. as a function of the angle of (c) α and (d) Re ; (e) lift and (f) drag coefficient r.m.s. in the $\alpha-Re$ parameter space. The zoom-in inset in panel (d) evidences the steep increase in r.m.s. near the secondary bifurcation at $\alpha = 8^\circ$. Symbols as in figure 3.

For $Re = 6000$, the maximum lift-to-drag ratio is obtained at $\alpha \approx 8^\circ$, in agreement with the results of Bauerheim & Chapin (2020). At these Re and α , the lift experiences a significant increase, while the drag has not yet experienced the large increase as for larger α . As found also by Bauerheim & Chapin (2020) for $Re = 6000$, the largest lift and drag coefficients, indeed, are reached at $\alpha \approx 10^\circ$.

Figure 24 depicts the root mean square (r.m.s.) of the lift and drag coefficients as a function of α (panels a and c) and Re (panels b and d). The lift and drag oscillations in the whole $\alpha-Re$ parameter space are also reported in figure 24(e, f) for a comprehensive visualisation. Figure 24(a, c) shows that for all Re , the lift- and drag-coefficient fluctuations are low in the $0^\circ \leq \alpha \leq 7^\circ$ range, while they become significant

for negative and large positive α . As shown in §5, this correlates well with the different nature of the secondary bifurcation. The fluctuations are indeed found to strongly intensify when the flow experiences a secondary bifurcation that leads to a change in the primary frequency of the limit cycles ($\alpha \leq -1.5^\circ$ and $\alpha > 7^\circ$), while a synchronous secondary bifurcation seems to affect less the lift/drag fluctuations ($-1.5^\circ < \alpha \leq 7^\circ$). The maximum lift fluctuation indeed occurs at $\alpha = -5^\circ$ for $Re = 2000$ when the flow experiences a secondary bifurcation due to the 2-D subharmonic mode, while the maximum drag fluctuation is found for $\alpha = 10^\circ$ at $Re \approx 4000$ after the 3-D subharmonic secondary bifurcation of the flow. This aspect is even more evident in figure 24(b, d). For example, at $\alpha = -5^\circ$, $\text{r.m.s.}(C'_l)$ ($\text{r.m.s.}(C'_d)$) increases from 0.05 (0.0015) to 0.22 (0.025) passing from $Re = 1450$ to $Re = 2000$, and then slightly decreases for higher Re . For $0^\circ \leq \alpha \leq 7^\circ$, instead, the fluctuations grow very weakly with Re and α : the maximum values, i.e. $\text{r.m.s.}(C'_l) = 0.017$ and $\text{r.m.s.}(C'_d) = 0.0032$, are found at $Re = 6000$ and $\alpha = 7^\circ$.

A last comment regards the largest Re and α considered. At $\alpha = 8^\circ$, $\text{r.m.s.}(C'_l)$ continues to increase with Re after the 3-D subharmonic bifurcation, while $\text{r.m.s.}(C'_d)$ reaches a plateau. For $\alpha \geq 9^\circ$, instead, after the wake three-dimensionalisation, the lift and drag oscillations reach a maximum and then weakly drop. This non-monotonic behaviour with Re at large $|\alpha|$, also found by Levy & Seifert (2009), is related to the complex vortex dynamics of this dragonfly-inspired geometry.

8. Conclusions and perspectives

In this study, we have investigated the sequence of bifurcations of the laminar flow past a dragonfly-inspired airfoil, using the geometry introduced by Newman *et al.* (1977). The angle of attack is varied in the range of $-5^\circ \leq \alpha \leq 10^\circ$ and Re is increased up to $Re = 6000$. We have used linear stability analyses to describe the primary and secondary bifurcations, and 2-D and 3-D direct numerical simulations to fully account for the nonlinear effects and detail the bifurcation scenario at larger Re . The aim of this work is to characterise the flow regimes that arise in the $\alpha-Re$ space of parameters, characterise the flow bifurcations and provide insights on the physics underlying the enhanced low- Re aerodynamic performance of corrugated airfoils compared with more common smooth airfoils.

The linear stability analysis shows that for all α , the flow experiences first a Hopf bifurcation, becoming unstable to oscillatory 2-D perturbations that lead to alternating vortex-shedding in the wake. Two different modes, namely mode pA and mode pC , are found to drive the primary instability for negative and positive α , respectively. The two modes are characterised by a different frequency and a distinct spatial structure. The structural sensitivity (Giannetti & Luchini 2007) shows that for mode pC , the wavemaker is localised in two lobes located downstream of the trailing-edge in the wake; mode pC is an unstable mode of the wake and resembles the classical von Kármán mode observed for common smooth airfoils (Gupta *et al.* 2023; Nastro *et al.* 2023). Mode pA , instead, is rather different. In this case, the structural sensitivity does not show a localised peak and the mode is relatively large along the bottom side of the airfoil. This suggests the existence of a non-local feedback in the triggering mechanism, which involves the recirculating regions that originate from the shear layer that separates at the bottom leading edge. The critical Re of the two modes decreases as $|\alpha|$ increases and for large positive and negative α , it is found to scale as a power law.

At intermediate Re , the flow approaches a periodic limit cycle for all α considered. Due to the complex geometry, different limit cycles arise, each one being characterised by a different vortex interaction. For positive α , the vortex shedding in the wake is governed

by the dynamics of the recirculating regions that arise over the top side of the airfoil. For negative α , instead, the vortex shedding is driven by the dynamics of the recirculating regions placed over the bottom side. Interestingly, for intermediate positive/negative α , the flow experiences vortex shedding from both the top/bottom LE and TE shear layers, and the two phenomena are frequency locked. This closely resembles what occurs for elongated rectangular cylinders (Okajima 1982; Chiarini *et al.* 2022b).

The nature of the secondary bifurcation changes with α , in agreement with the different 2-D limit cycles. Our results show that the secondary instability of the flow resembles what found for smooth airfoils (see Gupta *et al.* 2023) for large positive α only, where the wake dynamics dominates. For smaller α , instead, the nature of the secondary instability of the flow changes, being triggered by the complex dynamics of the vortices placed along the sides of the airfoil. The Floquet stability analysis reveals that the secondary bifurcation is 2-D for negative α and 3-D for positive ones. Like for the primary instability, the critical Re decreases as $|\alpha|$ increases. For intermediate negative α , the secondary bifurcation is associated with a pair of complex conjugate Floquet multipliers, which lead to a Neimark–Sacker bifurcation of the limit cycle: the flow remains 2-D but loses the temporal periodicity. For large negative α , instead, this branch of multipliers does not cross the unit circle and the secondary bifurcation is driven by an additional branch of real negative multipliers. For these α the secondary instability is 2-D and subharmonic. For positive α , several modes of different nature arise. For small α , the leading secondary mode is 3-D and synchronous. This is similar to what was found for bluff bodies, like circular (Barkley & Henderson 1996) and square (Robichaux *et al.* 1999) cylinders. However, unlike modes A and B of the circular and square cylinder case, the structural sensitivity localises the wavemaker of this mode in the recirculating region placed over the top side, indicating that the triggering mechanism is localised there and that it is related to the dynamics of the top-side vortices. For large positive α , instead, the secondary instability of the flow consists of a 3-D subharmonic bifurcation of the wake, similarly to what was found for smooth airfoils (Gupta *et al.* 2023).

The aerodynamic performance of the airfoil strongly depends on the flow regime. The mean lift coefficient is found to increase with α for all Re , whereas the mean drag coefficient shows a non-monotonic behaviour with respect to α , with the classical parabolic shape observed for small Re only. The largest lift-to-drag ratio is achieved at $\alpha = 8^\circ$ and $Re = 6000$. At these Re and α , the lift has largely increased, while the drag has not experienced yet the large increase as for higher α . The highest lift and drag coefficients are instead obtained for $Re = 6000$, but at the larger α of $\alpha \approx 10^\circ$. Notably, we found that the most significant changes in the time-averaged lift/drag values and in their corresponding fluctuations occur when the 2-D periodic wake transitions via a quasi-periodic or subharmonic secondary mode, i.e. the sSb and sQb modes for negative α , and the sS mode for high positive α . The wake transition via the synchronous sA mode for $-1.25^\circ < \alpha \leq 7^\circ$, instead, does not entail a significant change of the mean and fluctuations of the aerodynamic forces. In this range of intermediate α , the dragonfly-inspired airfoil provides thus a better capability to limit integral force oscillations with respect to other smooth airfoils (Levy & Seifert 2009).

The present study will serve as a starting point to further investigation. A natural extension of this work, of particular interest in the field of UAVs and MAVs, may include the finite wing effects and tandem wings. Another interesting extension would be to consider a moving corrugated airfoil to reproduce a flapping flight. This can be done in the spirit of the works by Jallas *et al.* (2017), which investigated the flow regimes past a pitching smooth airfoil, and Fujita & Iima (2023), which considered a corrugated airfoil and simplified the motion focusing on the unsteady lift generation by translating it from

rest. Moreover, of particular interest would be to assess the performance of the corrugated airfoils under unsteady conditions by simulating a gust encounter. During their operation, indeed, small-scale UAVs and MAVs are likely to encounter gusts that may also be of the order of the vehicle reference scale (Jones, Cetiner & Smith 2022). In this regard, the effect of stochastic inflow conditions on the flow regimes, and on the aerodynamic performances as well, should also be studied in a systematic manner. We also mention that a better understanding of the origin of the enhanced low- Re aerodynamic performances of these corrugated airfoils may be obtained by performing a force element analysis (Chang 1992), which allows to detect the origin of the aerodynamic loads (see also Ribeiro *et al.* 2022). Eventually, of particular interest would be to include the dynamics of the structure in the analysis.

Acknowledgements. G.N. would like to acknowledge M. Bauerheim for introducing the dragonfly-inspired geometry considered in this work to him on his arrival at ISAE-SUPAERO. Three-dimensional direct numerical simulations were performed using resources from GENCI [CCRT-CINES-IDRIS] (Grant A0122A07178) and from CALMIP (Grant 2022-p1425).

Funding. This research received no specific grant from any funding agency, commercial or not-for-profit sectors.

Declaration of interests. The authors report no conflict of interest.

Appendix A. Comparison with the work of Levy & Seifert (2009)

The dependence of the mean lift and drag coefficients on α is presented in figure 25 for $Re = 2000, 4000, 6000$. Results are compared with those obtained by Levy & Seifert (2009) (referred to as LS2009). In particular, the results on the dragonfly-inspired geometry are compared with those of three smooth airfoils: the Eppler-E61 airfoil whose aft-upper region surface is similar to the rear-upper part of the corrugated airfoil (see figure 1c of Levy & Seifert 2009), a ‘streamlined’ airfoil based on the closest streamline that circles the corrugated airfoil and the so-called ‘ v_0 -lined’ airfoil based on the contours created by the collection of points with a zero mean streamwise velocity, encompassing the separated flow regions (Levy & Seifert 2009).

The \overline{C}_l - α curves (figure 25a,c,e) show that the mean lift of the Eppler-E61 is approximately linear in the range of $-0.7^\circ < \alpha < 8$ regardless of the Reynolds number, while for the dragonfly-inspired geometry, increasing Re accentuates the deviation from the linear behaviour in the same range of α . As observed by Levy & Seifert (2009), the mean lift slope at $0^\circ < \alpha < 2^\circ$ is even larger than $2\pi \text{ rad}^{-1}$, in contrast to that of the Eppler-E61 ($\approx \pi \text{ rad}^{-1}$). The passing of the potential limit of $2\pi \text{ rad}^{-1}$ for the dragonfly-inspired periodic wing can be explained by the progressive growth of the separation regions in the forward part with α (both between and downstream of the two corrugations). This causes an effective increase in the airfoil camber with the angle of attack, resulting in overall higher lifting capability (Buckholtz 1986).

Interestingly, despite the lower lifting capabilities for a given α , figure 25 shows that the lift-to-drag ratio of the dragonfly-inspired wing might be superior to that of the smooth airfoils. At $Re = 6000$, for mean lift coefficient between 0 and 1, all smooth configurations considered exhibit a higher mean drag coefficient \overline{C}_D with respect to the dragonfly-inspired wing which thus provides higher lift-to-drag ratio.

Appendix B. Sensitivity to the computational grid

In this section, the sensitivity of the results to the domain size and grid resolution is investigated for both the primary and secondary bifurcations.

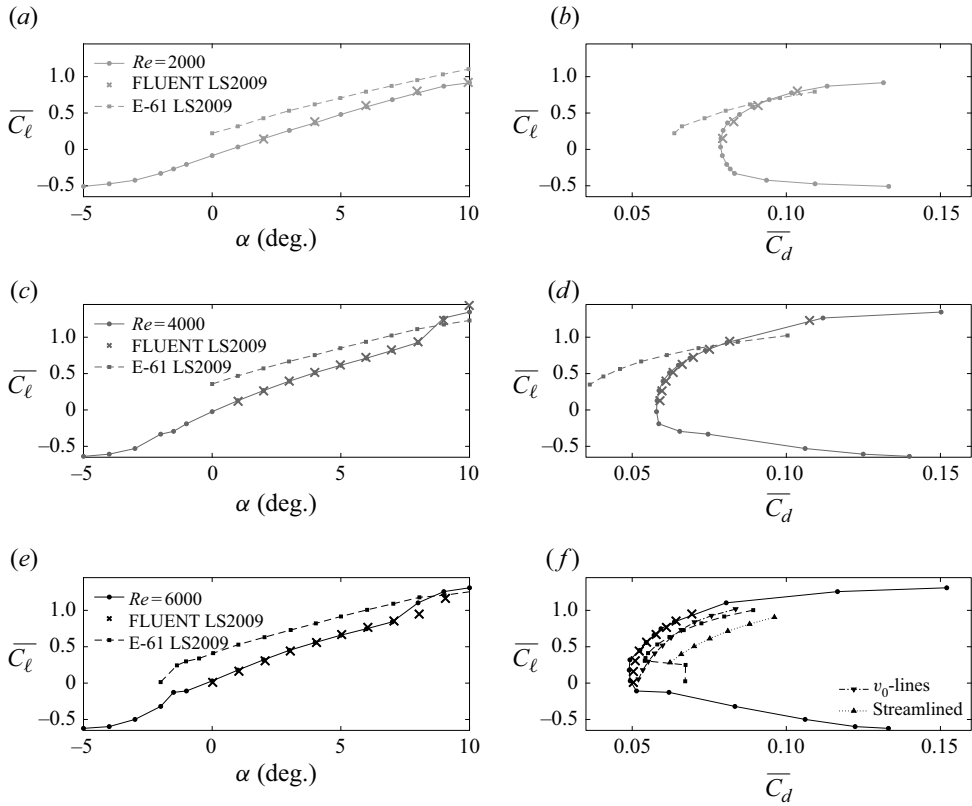


Figure 25. (a, c, e) Mean lift coefficient as a function of the angle of attack α . (b, d, f) Polar curves $\overline{C}_\ell - \overline{C}_d$. (a, b) $Re = 2000$; (c, d) $Re = 4000$; (e, f) $Re = 6000$. Comparison with the results of Levy & Seifert (2009) (referred to as LS2009).

B.1. Primary bifurcation

We have examined the influence of the grid resolution on the frequency f_{DNS} from nonlinear simulations, the growth rate σ_1 and the frequency $f_1 = \omega_1/2\pi$ of the leading primary instability developing on the dragonfly-inspired airfoil at different α and Re . Polynomial order convergence on a two-dimensional computational domain extending for $(\ell_x, \ell_y) = (20c, 20c)$ has been verified to assess the mesh requirement, and some results are summarised in table 2. The total number of degrees of freedom N_{dof} is 3.58×10^6 for $P = 4$, $N_{dof} = 8.06 \times 10^6$ for $P = 6$ and $N_{dof} = 1.43 \times 10^7$ for $P = 8$. The analysis of the polynomial order on the grid shows that the numerical convergence is substantially reached since the relative error is always lower than $\sim 1\%$.

B.2. Secondary bifurcation

We have investigated the dependence of the results on the grid size and grid resolution by repeating the complete Floquet analysis by varying the extent of the computational domain and the grid resolution. The convergence study has been performed for three different angles of attack, $\alpha = 10^\circ$ and $\alpha = -5^\circ$ (the extrema of the range of α considered in this work) and $\alpha = 7^\circ$. This allows us to consider the different growing modes detected in § 6, i.e. mode sS for $\alpha = 10^\circ$, mode sA for $\alpha = 7^\circ$, and modes $sQPb$ and $sS2$ for $\alpha = -5^\circ$.

α	Re	P	N_{dof}	St_{DNS}	σ_1	$f_1 = \omega_1/2\pi$
10°	815	4	3.58×10^6	0.9441	1.7021×10^{-2}	0.9417
10°	815	6	8.06×10^6	0.9436	1.6882×10^{-2}	0.9418
10°	815	8	1.43×10^7	0.9434	1.6801×10^{-2}	0.9418
5°	2000	4	3.58×10^6	1.7140	1.8242×10^{-1}	1.6107
5°	2000	6	8.06×10^6	1.6954	1.8266×10^{-1}	1.6107
5°	2000	8	1.43×10^7	1.6948	1.8271×10^{-1}	1.6107
0°	2925	4	3.58×10^6	1.8672	3.3571×10^{-3}	1.8612
0°	2925	6	8.06×10^6	1.8635	3.5395×10^{-3}	1.8610
0°	2925	8	1.43×10^7	1.8618	3.5709×10^{-3}	1.8610
-5°	1200	4	3.58×10^6	1.0009	6.2568×10^{-2}	0.9825
-5°	1200	6	8.06×10^6	0.9969	6.0730×10^{-2}	0.9822
-5°	1200	8	1.43×10^7	0.9968	6.0227×10^{-2}	0.9821

Table 2. Frequency St_{DNS} from nonlinear simulations, growth rate σ_1 and frequency $f_1 = \omega_1/2\pi$ of the leading primary instability developing on the dragonfly-inspired airfoil at different α and Re for different polynomial orders P on a two-dimensional computational domain extending for $(\ell_x, \ell_y) = (20c, 20c)$.

α	Re	β	ℓ_x	ℓ_y	N_{el}	St_{BF}	μ
10°	1700	50	17.5	7	92×10^3	1.3302	(-0.802, 0)
10°	1700	50	17.5	10	11.5×10^4	1.3447	(-0.711, 0)
10°	1700	50	17.5	14	13.8×10^4	1.3582	(-0.637, 0)
10°	1700	50	17.5	20	14.1×10^4	1.3687	(-0.581, 0)
10°	1700	50	17.5	25	13.9×10^4	1.3751	(-0.548, 0)
10°	1700	50	17.5	30	13.1×10^4	1.3778	(-0.534, 0)
10°	1700	50	17.5	35	12.2×10^4	1.3792	(-0.528, 0)
10°	1700	50	20	25	15.2×10^4	1.3714	(-0.567, 0)
10°	1700	50	22.5	25	15.9×10^4	1.3702	(-0.572, 0)
7°	4500	20	17.5	14	13.8×10^4	2.3764	(1.0557, 0)
7°	4500	20	20	30	15.4×10^4	2.3624	(1.0612, 0)
-5°	1450	0	17.5	14	13.8×10^4	1.0738	(0.7458, 0.6514)
-5°	1450	0	20	30	15.4×10^4	1.0710	(0.7539, 0.6529)
-5°	1450	0	17.5	14	13.8×10^4	1.0738	(-0.9281, 0.1171)
-5°	1450	0	20	30	15.4×10^4	1.0710	(-0.8972, 0.1571)

Table 3. Dependence of the Floquet multiplier on the size of the computational domain for $\alpha = 10^\circ$ (with $Re = 1700$ and $\beta = 50$), $\alpha = 7^\circ$ (with $Re = 4500$ and $\beta = 20$) and $\alpha = -5^\circ$ (with $Re = 1450$ and $\beta = 0$). The baseline grid for $8^\circ \leq \alpha \leq 10^\circ$ has $\ell_y = 30$, $\ell_x = 20$ and $N_{el} = 15.4 \times 10^4$. The baseline grid for $-5^\circ \leq \alpha \leq 7^\circ$ has $\ell_x = 14$, $\ell_x = 17.5$ and $N_{el} = 13.8 \times 10^4$.

For $\alpha = 10^\circ$, the streamwise extent of the computational domain has been varied between $\ell_x = 17.5$ and $\ell_x = 22.5$, while the vertical extent between $\ell_y = 7$ and $\ell_y = 35$ (recall that all quantities are made dimensionless using the airfoil chord c as length scale). For all the grids, the grid resolution close to the body is maintained approximately

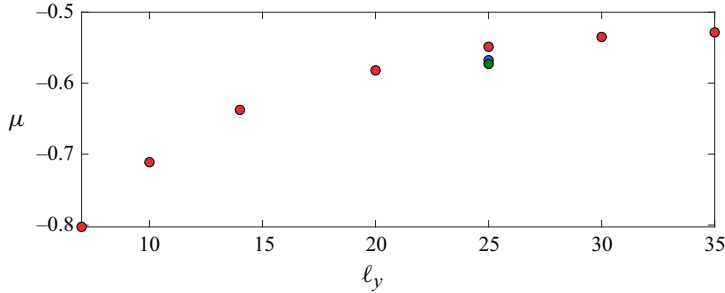


Figure 26. Dependence of the Floquet multiplier on the size of the domain for $\alpha = 10^\circ$, $Re = 1700$ and $\beta = 50$. The red circle is for $\ell_x = 17.5$, the blue circle is for $\ell_x = 20$ and the green circle is for $\ell_x = 22.5$.

constant. In this case, we have considered $Re = 1700$ and $\beta = 50$. When fixing $\ell_x = 17.5$, an increase of the vertical extent of the computational domain from $\ell_y = 7$ to $\ell_y = 35$ leads to a variation of the base flow frequency of $|\Delta St_{BF}| \approx 3.5\%$, and to a variation of the multiplier associated with mode sS of $|\Delta |\mu_{sS}|| \approx 34.16\%$ (see table 3 and figure 26). In contrast, when fixing the vertical extent of the grid to $\ell_y = 25$, an increase of the streamwise extent from $\ell_x = 17.5$ to $\ell_x = 22.5$ leads to $|\Delta St_{BF}| \approx 0.35\%$ and $|\Delta |\mu_{sS}|| \approx 4\%$. Based on this convergence study, for $\alpha = 10^\circ$, we have chosen $(\ell_x, \ell_y) = (20, 30)$ with a number of elements $N_{el} \approx 15.4 \times 10^4$, after having verified that an increase of the grid resolution ($N_{el} \approx 18.5 \times 10^4$) leads to a negligible variation ($\lesssim 1\%$) of the results.

For the smaller angles of attack, instead, we have considered $Re = 4500$ and $\beta = 20$ (for $\alpha = 7^\circ$), and $Re = 1450$ and $\beta = 0$ (for $\alpha = -5^\circ$). This enables us to investigate the sensitivity of modes sA , $sQPb$ and $sS2$ on the grid. For these α , two grids have been considered. The baseline grid used for $\alpha = 10^\circ$ (with $\ell_x = 20$ and $\ell_y = 30$) and a smaller grid with $(\ell_x, \ell_y) = (17.5, 14)$; see table 3. For $\alpha = 7^\circ$, we found a variation of $|\Delta St_{BF}| \approx 0.59\%$ and $|\Delta |\mu_{sA}|| \approx 0.51\%$. For $\alpha = -5^\circ$, instead, we measure a variation of $|\Delta St_{BF}| \approx 0.26\%$, $|\Delta |\mu_{sS2}|| \approx 2.6\%$ and $|\Delta |\mu_{sQPb}|| \approx 0.71\%$. Based on these results and given that the nature of the different modes are well described by all the considered grids, for $-5^\circ \leq \alpha \leq 7^\circ$, we have adopted the smaller grid with $\ell_x = 17.5$ and $\ell_y = 14$, with $N_{el} = 13.8 \times 10^4$. We have verified the adequacy of the grid resolution using $\alpha = 7^\circ$ and mode sA as reference. We have increased the number of elements to $N_{el} = 15.8 \times 10^4$ and $N_{el} = 18.7 \times 10^4$ (mainly in the near wake and close to the body) and observed a marginal variation ($\lesssim 1\%$) of the results.

REFERENCES

- ÅKERVIK, E., BRANDT, L., HENNINGSON, D.S., HEPFFNER, J., MARXEN, O. & SCHLATTER, P. 2006 Steady solutions of the Navier–Stokes equations by selective frequency damping. *Phys. Fluids* **18** (6), 068102.
- BARKLEY, D. & HENDERSON, R.D. 1996 Three-dimensional Floquet stability analysis of the wake of a circular cylinder. *J. Fluid Mech.* **322**, 215–241.
- BARKLEY, D., TUCKERMAN, L.S. & GOLUBITSKY, M. 2000 Bifurcation theory for three-dimensional flow in the wake of a circular cylinder. *Phys. Rev. E* **61** (5), 5247–5252.
- BAUERHEIM, M. & CHAPIN, V. 2020 Route to chaos on a dragonfly wing cross section in gliding flight. *Phys. Rev. E* **102** (1), 011102.
- BLACKBURN, H.M. & LOPEZ, J.M. 2003 On three-dimensional quasiperiodic Floquet instabilities of two-dimensional bluff body wakes. *Phys. Fluids* **15** (8), L57–L60.
- BLACKBURN, H.M., MARQUES, F. & LOPEZ, J.M. 2005 Symmetry breaking of two-dimensional time-periodic wakes. *J. Fluid Mech.* **522**, 395–411.
- BOGHOSIAN, M.E. & CASSEL, K.W. 2016 On the origins of vortex shedding in two-dimensional incompressible flows. *Theor. Comput. Fluid Dyn.* **30** (6), 511–527.

- BOMPHELY, R.J., NAKATA, T., HENNINGSSON, P. & LIN, H.-T. 2016 Flight of the dragonflies and damselflies. *Phil. Trans. R. Soc. Lond. B: Biol. Sci.* **371** (1704), 20150389.
- BUCKHOLTZ, R.H. 1986 The functional role of wing corrugations in living systems. *J. Fluids Engng* **108** (93), 93–97.
- CHANG, C.-C. 1992 Potential flow and forces for incompressible viscous flow. *Proc. R. Soc. Lond. A* **437** (1901), 517–525.
- CHIARINI, A. & AUTERI, F. 2023 Linear global and asymptotic stability analysis of the flow past rectangular cylinders moving along a wall. *J. Fluid Mech.* **966**, A22.
- CHIARINI, A. & BOUJO, E. 2024 Stability and dynamics of the laminar flow past rectangular prisms. arXiv: 2405.04705.
- CHIARINI, A., QUADRIO, M. & AUTERI, F. 2021 Linear stability of the steady flow past rectangular cylinders. *J. Fluid Mech.* **929**, A36.
- CHIARINI, A., QUADRIO, M. & AUTERI, F. 2022a An almost subharmonic instability in the flow past rectangular cylinders. *J. Fluid Mech.* **950**, A20.
- CHIARINI, A., QUADRIO, M. & AUTERI, F. 2022b On the frequency selection mechanism of the low-Re flow around rectangular cylinders. *J. Fluid Mech.* **933**, A44.
- CHOI, C.-B. & YANG, K.-S. 2014 Three-dimensional instability in flow past a rectangular cylinder ranging from a normal flat plate to a square cylinder. *Phys. Fluids* **26** (6), 061702.
- CHOMAZ, J.-M. 2005 Global instabilities in spatially developing flows: non-normality and nonlinearity. *Annu. Rev. Fluid Mech.* **37** (1), 357–392.
- CITRO, V., LUCHINI, P., GIANNETTI, F. & AUTERI, F. 2017 Efficient stabilization and acceleration of numerical simulation of fluid flows by residual recombination. *J. Comp. Phys.* **344**, 234–246.
- DENG, J., SUN, L. & SHAO, X. 2017 Floquet stability analysis in the wake of a NACA0015 airfoil at post-stall angles of attack. *Phys. Fluids* **29** (9), 094104.
- FAGE, A. & JOHANSEN, F.C. 1927 On the flow of air behind an inclined flat plate of infinite span. *Proc. R. Soc. Lond. A* **116** (773), 170–197.
- FISCHER, P.F., LOTTES, J.W. & KERKEMEIER, S.G. 2008 Nek5000 web page. Available at <http://nek5000.mcs.anl.gov>.
- FRANTZ, R.A.S., LOISEAU, J.-CH & ROBINET, J.-CH 2023 Krylov methods for large-scale dynamical systems: application in fluid dynamics. *Appl. Mech. Rev.* **75** (3), 030802.
- FUJITA, Y. & IMA, M. 2023 Dynamic lift enhancement mechanism of dragonfly wing model by vortex-corrugation interaction, *Phys. Rev. Fluids* **8** (12), 123101.
- GIANNETTI, F., CAMARRI, S. & LUCHINI, P. 2010 Structural sensitivity of the secondary instability in the wake of a circular cylinder. *J. Fluid Mech.* **651**, 319–337.
- GIANNETTI, F. & LUCHINI, P. 2007 Structural sensitivity of the first instability of the cylinder wake. *J. Fluid Mech.* **581**, 167–197.
- GUPTA, S., ZHAO, J., SHARMA, A., AGRAWAL, A., HOURIGAN, K. & THOMPSON, M.C. 2023 Two- and three-dimensional wake transitions of a NACA0012 airfoil, *J. Fluid Mech.* **954**, A26.
- HAMMOND, D.A. & REDEKOPP, L.G. 1997 Global dynamics of symmetric and asymmetric wakes. *J. Fluid Mech.* **331**, 231–260.
- HE, W., GIORIA, R.S., PÉREZ, J.M. & THEOFILIS, V. 2017 Linear instability of low Reynolds number massively separated flow around three NACA airfoils. *J. Fluid Mech.* **811**, 701–741.
- HECHT, F. 2012 New development in freefem++. *J. Numer. Maths* **20** (3-4), 251–266.
- HOIRIGAN, K., THOMPSON, M.C. & TAN, B.T. 2001 Self-sustained oscillations in flows around long blunt plates. *J. Fluids Struct.* **15** (3), 387–398.
- JACKSON, C.P. 1987 A finite-element study of the onset of vortex shedding in flow past variously shaped bodies. *J. Fluid Mech.* **182**, 23–45.
- JALLAS, D., MARQUET, O. & FABRE, D. 2017 Linear and nonlinear perturbation analysis of the symmetry breaking in time-periodic propulsive wakes. *Phys. Rev. E* **95** (6-1), 063111.
- JONES, A.R., CETINER, O. & SMITH, M.J. 2022 Physics and modeling of large flow disturbances: discrete gust encounters for modern air vehicles. *Annu. Rev. Fluid Mech.* **54** (1), 469–493.
- JONGERIUS, S.R. & LENTINK, D. 2010 Structural analysis of a dragonfly wing. *Expl. Mech.* **50** (9), 1323–1334.
- KANG, C.-K. & SHYY, W. 2013 Scaling law and enhancement of lift generation of an insect-size hovering flexible wing. *J. R. Soc. Interface* **10** (85), 20130361.
- VON KÁRMÁN, T. 1954 *Aerodynamics*. McGraw-Hill.
- KESEL, A.B. 2000 Aerodynamic characteristics of dragonfly wing sections compared with technical aerofoils. *J. Exp. Biol.* **203** (20), 3125–3135.
- LEONTINI, J.S., LO JACONO, D. & THOMPSON, M.C. 2015 Stability analysis of the elliptic cylinder wake. *J. Fluid Mech.* **763**, 302–321.

- LEVY, D.-E. & SEIFERT, A. 2009 Simplified dragonfly airfoil aerodynamics at Reynolds numbers below 8000. *Phys. Fluids* **21** (7), 071901.
- LIU, H., RAVI, S., KOLOMENSKIY, D. & TANAKA, H. 2016 Biomechanics and biomimetics in insect-inspired flight systems. *Phil. Trans. R. Soc. Lond. B: Biol. Sci.* **371** (1704), 20150390.
- MARQUET, O. & LARSSON, M. 2015 Global wake instabilities of low aspect-ratio flat-plates. *Eur. J. Mech. B Fluids* **49**, 400–412.
- MENEGHINI, J.R., CARMO, B.S., TSILOUFAS, S.P., GIORIA, R.S. & ARANHA, J.A.P. 2011 Wake instability issues: from circular cylinders to stalled airfoils. *J. Fluids Struct.* **27** (5), 694–701.
- MILLS, R., SHERIDAN, J., HOURIGAN, K. & WELSH, M.C. 1995 The mechanism controlling vortex shedding from rectangular bluff bodies. In *Proceedings of the 20th Australasian Fluid Mechanics Conference*, pp. 227–230.
- MONKEWITZ, P.A., HUERRE, P. & CHOMAZ, J.-M. 1993 Global linear stability analysis of weakly non-parallel shear flows. *J. Fluid Mech.* **251**, 1–20.
- NAKAMURA, Y. & NAKASHIMA, M. 1986 Vortex excitation of prisms with elongated rectangular, H and [vdash] cross-sections. *J. Fluid Mech.* **163**, 149–169.
- NASTRO, G., FONTANE, J. & JOLY, L. 2020 Optimal perturbations in viscous round jets subject to Kelvin–Helmholtz instability. *J. Fluid Mech.* **900**, A13.
- NASTRO, G., ROBINET, J.-CH, LOISEAU, J.-CH, PASSAGGIA, P.-Y. & MAZELLIER, N. 2023 Global stability, sensitivity and passive control of low-Reynolds-number flows around NACA 4412 swept wings. *J. Fluid Mech.* **957**, A5.
- NEWMAN, B.G., SAVAGE, S.B. & SCHOUELLA, D. 1977 Model test on a wing section of a dragonfly. In *Scale Effects in Animal Locomotion* (ed. T. J. Pedley), pp. 445–477. London: Academic Press.
- OKAJIMA, A. 1982 Strouhal numbers of rectangular cylinders. *J. Fluid Mech.* **123**, 379–398.
- OKAMOTO, M., YASUDA, K. & AZUMA, A. 1996 Aerodynamic characteristics of the wings and body of a dragonfly. *J. Exp. Biol.* **199** (2), 281–294.
- PHAN, H.V. & PARK, H.C. 2019 Insect-inspired, tailless, hover-capable flapping-wing robots: recent progress, challenges, and future directions. *Prog. Aerosp. Sci.* **111**, 100573.
- RAI, M.M. & MOIN, P. 1991 Direct simulations of turbulent flow using finite-difference schemes. *J. Comput. Phys.* **96** (1), 15–53.
- RIBEIRO, J.H.M., YEH, C.-A., ZHANG, K. & TAIRA, K. 2022 Wing sweep effects on laminar separated flows. *J. Fluid Mech.* **950**, A23.
- ROBICHAUX, J., BALACHANDAR, S. & VANKA, S.P. 1999 Three-dimensional Floquet instability of the wake of square cylinder. *Phys. Fluids* **11** (3), 560–578.
- RYAN, K., THOMPSON, M.C. & HOURIGAN, K. 2005 Three-dimensional transition in the wake of bluff elongated cylinders. *J. Fluid Mech.* **538**, 1–29.
- RÜPPELL, G. 1989 Kinematic analysis of symmetrical flight manoeuvres of odonata. *J. Exp. Biol.* **144** (1), 13–42.
- SAAD, Y. 2011 *Numerical Methods for Large Eigenvalue Problems*. Society for Industrial and Applied Mathematics.
- SREENIVASAN, K.R., STRYKOWSKI, P.J. & OLINGER, D.J. 1987 Hopf bifurcation, Landau equation, and vortex shedding behind circular cylinders. In *Proceedings of the Forum on Unsteady Flow Separation* (ed. K. Ghia), vol. 52, pp. 1–13. ASME.
- THEOFILIS, V. 2003 Advances in global linear instability analysis of nonparallel and three-dimensional flows. *Prog. Aerosp. Sci.* **39** (4), 249–315.
- THEOFILIS, V. 2011 Global linear instability. *Annu. Rev. Fluid Mech.* **43** (1), 319–352.
- THOMPSON, M.C., LEWEKE, T. & WILLIAMSON, C.H.K. 2001 The physical mechanism of transition in bluff body wakes. *J. Fluids Struct.* **15** (3), 607–616.
- WAKELING, J.M. & ELLINGTON, C.P. 1997 Dragonfly flight: I. Gliding flight and steady-state aerodynamic forces. *J. Exp. Biol.* **200** (3), 543–556.
- WILLIAMSON, C.H.K. 1988 The existence of two stages in the transition to three-dimensionality of a cylinder wake. *Phys. Fluids* **31** (11), 3165–3168.
- YANG, D., PETTERSEN, B., ANDERSSON, H.I. & NARASIMHAMURTHY, V.D. 2013 Floquet stability analysis of the wake of an inclined flat plate. *Phys. Fluids* **25** (9), 094103.
- ZAMPOGNA, G.A. & BOUJO, E. 2023 From thin plates to Ahmed bodies: linear and weakly nonlinear stability of rectangular prisms. *J. Fluid Mech.* **966**, A19.